POLITECNICO DI TORINO
Repository ISTITUZIONALE

A two-soil-layer agro-hydrological model for irrigation requirements: Evaluation and trends in the Po River basin

Original
A two-soil-layer agro-hydrological model for irrigation requirements: Evaluation and trends in the Po River basin / Shahmohammadi, A., Tamea, S.. - In: AGRICULTURAL WATER MANAGEMENT. - ISSN 0378-3774. - 338:(2026). [10.1016/j.agwat.2026.110887]

Availability:
This version is available at: 11583/3017584 since: 2026-11-05T12:13:18Z

Publisher:
Elsevier

Published
DOI:10.1016/j.agwat.2026.110887

Terms of use:

This article is made available under terms and conditions as specified in the corresponding bibliographic description in the repository

Publisher copyright

(Article begins on next page)

15 November 2026

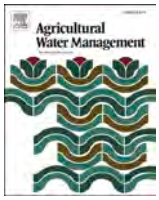
Agricultural Water Management 338 (2026) 110887



Contents lists available at ScienceDirect

Agricultural Water Management

journal homepage: www.elsevier.com/locate/agwat



A two-soil-layer agro-hydrological model for irrigation requirements: Evaluation and trends in the Po River basin

Amirarsalan Shahmohammadi *, Stefania Tamea

Department of Environment, Land and Infrastructure Engineering, Politecnico di Torino, Corso Duca degli Abruzzi, 24, Turin, 10129, Italy

ARTICLE INFO

Handling Editor: Ranvir Singh

Keywords:
Crop water demand
Irrigated Agriculture
Northern Italy
Hydroclimatic drivers
Irrigation Scheduling
Phenological sensitivity

ABSTRACT

Increasing hydrological and agricultural droughts in the Po River Basin in northern Italy, one of the most intensively irrigated agricultural regions in Europe, have raised growing concerns about water resources management and highlighted the need for accurate estimates of irrigation requirements (*IR*). This study presents AGRHYD, a two-compartment (topsoil–subsoil) soil-water balance model built on the FAO 56 dual crop coefficient approach to estimate crop actual evapotranspiration ($ET_{c\ act}$), crop evapotranspiration (ET_c) and *IR* at point and regional scales. The explicit topsoil compartment, responsible for soil evaporation, facilitates future reconciliation and integration with satellite-based soil moisture retrievals. Since *IR* is a theoretical construct and cannot be directly measured, the model's daily $ET_{c\ act}$ estimates for wheat and vine, two of the typical rainfed crops in the region, were evaluated against two independent satellite-based evapotranspiration products, WaPOR and GLEAM yielding Pearson's correlation coefficient (*r*) up to 0.88 and an RMSE as low as 0.91 mm day^{-1} for wheat, and *r* up to 0.91 and an RMSE as low as 0.58 mm day^{-1} for vine, with satisfactory reproduction of $ET_{c\ act}$ temporal dynamics at daily, seasonal, and annual scales. *IR* was subsequently estimated for maize and forages, two of the main irrigated crops in the region, over the period 1981–2022, revealing pronounced spatial heterogeneity with the highest demands concentrated in eastern Piedmont and Emilia-Romagna. Long-term trend analysis identified statistically significant increasing trends in annual *IR* across the basin with mean rates of 0.88 mm year^{-1} for maize and 1.17 mm year^{-1} for forages, driven primarily by trends in June and July. Concurrent declining precipitation and increasing crop reference evapotranspiration (ET_o) across the basin during these months broadly provide a physically consistent hydroclimatic explanation. A sensitivity analysis confirmed that the key trend findings are robust to uncertainty in crop calendar timing. The resulting *IR* dataset and long-term trend diagnostics constitute a valuable resource for irrigation planning and water allocation in the Po River Basin, while the model's reliable performance and modest data requirements make it transferable to other irrigated regions.

1. Introduction

The largest proportion of freshwater withdrawals is attributed to irrigation water demand in agriculture (FAO, 2020a). This demand is expected to increase due to more frequent and severe droughts driven by climate change, which put rainfed cultivation under pressure, thereby raising the need for irrigation and expanding the area of croplands equipped for irrigation worldwide (FAO, 2024). This situation is further exacerbated by concerns related to food security and the need to meet growing food demand due to the rising global population (FAO, 2020a), potentially leading to a 50% increase in irrigated agriculture by 2050 (Food and Agriculture Organization of the United Nations, 2020). Sophocleous (2004) projected that by 2025, freshwater withdrawal could rise to 70–90% of accessible resources, primarily due to agricultural use. However, by 2021, this figure had already surpassed 90% in 28 countries (FAO, 2024). These trends underscore, among other concerns, the critical need to evaluate the amount of freshwater required for irrigation (Döll and Siebert, 2002), and to adopt more efficient irrigation practices within the broader framework of sustainable water resource management, in order to alleviate pressure on freshwater resources and safeguard both food production and freshwater availability (Rockström et al., 2010).

The minimum amount of water that must be supplied to crops, beyond what precipitation provides, needed to achieve optimal crop

* Corresponding author.
E-mail address: amirarsalan.shahmohammadi@polito.it (A. Shahmohammadi).

https://doi.org/10.1016/j.agwat.2026.110887
Received 6 April 2026; Received in revised form 12 October 2026; Accepted 19 October 2026
Available online 5 November 2026
0378-3774/© 2026 The Authors. Published by Elsevier B.V. This is an open access article under the CC BY license (http://creativecommons.org/licenses/by/4.0/).

productivity, is referred to as Irrigation Requirements (*IR*) (Allen et al., 1998; Natural Resources Conservation Service, 1997). In other words, *IR* is determined by the difference between precipitation and the crop water use rate under optimal productivity conditions (Allen et al., 1998). However, *IR* is not a physical quantity that can be directly observed or recorded with instruments; rather, it is a theoretical construct that can be derived based on the crop water use rate under optimal conditions, represented by the crop evapotranspiration (ET_c). Yet ET_c is itself a theoretical upper bound for crop water use and cannot be measured. Crop actual evapotranspiration ($ET_{c\ act}$), which represents crop water use under real field conditions including water stress, can however be measured or estimated using different methods and where water stress is absent, $ET_{c\ act}$ converges to ET_c, enabling *IR* estimation. $ET_{c\ act}$ can be measured in the field using two main approaches: mass balance methods (e.g., lysimeters) and micrometeorological methods (e.g., eddy covariance systems). These are considered highly reliable and accurate (Hillel et al., 2005), but they are also expensive and time-consuming, with limitations such as limited spatial representativeness (Allen et al., 1998; Natural Resources Conservation Service, 1997), particularly in large-scale studies (i.e., regional or basin scale). To address these challenges, $ET_{c\ act}$ can also be estimated through a variety of alternative methods, namely: (1) physically based approaches, (2) soil-water balance (SWB) models, (3) remote sensing-based techniques, and more recently, (4) methods utilizing machine learning.

In physically based approaches, the Penman–Monteith (P-M) and the Priestley–Taylor (P-T) methods are the most widely used for estimating $ET_{c\ act}$ (McColl, 2020; Sumner and Jacobs, 2005), as they incorporate both energy balance parameters (i.e., net radiation, soil heat flux) and mass transfer factors (i.e., surface and aerodynamic resistance). In P-M method, however, parameterizing the resistance terms remains challenging (Xiong et al., 2019), while the P-T method uses an empirical coefficient to bypass these challenges, yet this coefficient varies with local conditions and depends on several environmental factors (Gavin and Agnew, 2004; Sumner and Jacobs, 2005).

SWB models estimate $ET_{c\ act}$ as the residual of a linear relationship between soil water components and water inputs to the soil. Steady-state SWB models operate on a fixed time step (typically one day), assuming that system conditions remain stable during that period. In contrast, transient-state SWB models are more complex, accounting for continuously varying conditions over time (Pereira et al., 2020). However, accurately estimating $ET_{c\ act}$ using SWB models requires knowledge of soil moisture—among other factors—which is a challenging parameter to obtain, particularly at scales beyond a point measurement or small agricultural field.

Advances in remote sensing techniques have led to the development of models capable of directly estimating $ET_{c\ act}$ in a cost-effective and spatially distributed manner across regional and global scales, primarily leveraging satellite-derived data (Xue et al., 2025). According to FAO (2023), the most operational remote sensing-based models to estimate $ET_{c\ act}$ can be categorized into three groups: Surface Energy Balance (SEB), P-M, and Satellite Psychrometric Approach (SPA) which were applied in the literature (Dias Lopes et al., 2019; García-Gutiérrez et al., 2021; Ma et al., 2023; Oliveira et al., 2024; Senay et al., 2022; Singh and Senay, 2016; Sun et al., 2011). SEB- and SPA-based models rely on satellite-derived land surface temperature, which is only available under cloud-free conditions. Cloud masking techniques mitigate this issue but they are accompanied by uncertainties from aerosols, dust, and smoke while cause spatial gaps and temporal discontinuities due to the exclusion of unclear pixels. These models also require interpolating instantaneous $ET_{c\ act}$ values from satellite overpasses to daily estimates, assuming constant $ET_{c\ act}$ —a simplification that fails under episodic precipitation or irrigation (FAO, 2023). P-M-based models address cloud limitations by solving the P-M equation daily using various satellite inputs, including microwave data, though this increases complexity due to additional parameter requirements. Two recent global remote sensing-based land evapotranspiration products which employ P-M equation are WaPOR (FAO, 2020b) and GLEAM (Miralles et al., 2025) where on agricultural fields they represent $ET_{c\ act}$. WaPOR solves the P-M equation separately for transpiration (*Tr*) and soil evaporation (*E*) using remote sensing inputs in a complex framework, providing global high resolution (i.e., 300 m) dekadal to annual data. GLEAM estimates potential evapotranspiration using the P-M equation, adjusting it with environmental stress factors (e.g. soil moisture), producing global *Tr* and *E* data at 0.1° (~ 11 km) resolution.

Machine learning techniques have improved the accuracy of $ET_{c\ act}$ estimation at both field and regional scales (Dong et al., 2022; Xue et al., 2025), largely due to advances in deep learning models (Feng et al., 2024; Yan et al., 2023). Nevertheless, these approaches typically require large volumes of high-quality training data, which are often unavailable. In addition, their currently high computational demands pose practical limitations, restricting the broader application of such techniques.

Among these, the Food and Agriculture Organization (FAO) provides a widely adopted combined method known as FAO 56 (Allen et al., 1998) integrating a physically based method (i.e., P-M) and empirical crop and soil characteristics to estimate $ET_{c\ act}$ while using an SWB model to account for water availability for the crop. It parameterizes the P-M equation (i.e., FAO P-M) to estimate a crop reference evapotranspiration (ET_0) which is multiplied by a coefficient representing combined crop and soil characteristics, and a water stress coefficient derived from the SWB yielding crop. This is known as FAO 56 single crop coefficient (single-K_c) approach. However, $ET_{c\ act}$ can be obtained also by estimating *Tr* and *E* separately by isolating crop characteristics from those of soil which is known as FAO 56 dual crop coefficient (dual-K_c) approach. The FAO 56 method is considered robust and relatively simple to implement (Fereres and Soriano, 2007), utilizing commonly available meteorological variables (e.g. temperature, precipitation, and solar radiation) (Droogers and Allen, 2002). It is standardized across climates and crops (Allen et al., 1998) and has empirical flexibility for a variety of environmental contexts (Pereira et al., 2015). Nevertheless, some limitations have been reported including the need for local calibration of crop characteristics under high atmospheric demand (Marin et al., 2019); errors in ET_0 estimation due to missing or poor-quality meteorological data; the temporal and spatial variability of ET_0 in relation to climate variables; and inaccurate $ET_{c\ act}$ estimates under deficit irrigation conditions (Cid et al., 2018).

The methods discussed above are primarily developed to estimate $ET_{c\ act}$. However, as discussed earlier, under no water stress condition, $ET_{c\ act}$ converges to ET_c, enabling *IR* estimation. It should be noted, however, that remote sensing-based products usually provide estimate on $ET_{c\ act}$ under actual field conditions including water stress, and therefore require additional assumptions or modifications to derive ET_c, whereas SWB models such as FAO 56 can directly yield ET_c by assuming optimal water supply conditions. Once an adequate estimate of ET_c is obtained using one of the methods discussed earlier, *IR* can be determined.

At the global scale, several studies have attempted to address the need for *IR* data by applying the FAO 56 method, or an extended version of it, to estimate evapotranspiration , combined with various methods for estimating ET_0 or using multi-module hydrological models based on the SEB. These studies have provided global *IR* data for different crops at varying spatial and temporal resolutions, accounting for climate-driven interannual variability, partitioning *Tr* from *E*, crop water footprint, and yield, while utilising meteorological data with annual, monthly, and daily temporal resolutions. For more information on these efforts, see (Rolle et al., 2021). These studies primarily used a base year from which irrigated and harvested areas were adopted and assumed to remain constant for other years. In the most recent effort, (Mialyk et al., 2024) provided global data by applying a modified version of the AquaCrop model—an extended version of the FAO 56 method—that accounts for the temporal dynamics of crops and irrigated areas.

At the regional and basin scale, several studies have provided insights and data on $ET_{c\ act}$ and *IR* from diverse regions across the globe

(Aus der Beek et al., 2010; Bastiaanssen et al., 2002; Geng et al., 2023; Nie et al., 2021; Parmar et al., 2023; Ruess et al., 2023). These studies employed the methods discussed earlier—either individually or in combination—with remote sensing-based approaches being more frequently used (El-Magd and Tanton, 2005; Folhes et al., 2009; Parmar et al., 2023; Xue et al., 2021) compared to global studies. Among the regions where *IR* assessment is particularly critical, Mediterranean Europe stands out as an agricultural hotspot facing intensifying hydro-climatic pressures (Granata et al., 2025). This region, which dominates the production of certain crops, makes a substantial contribution to overall agricultural output in Europe (Cook, 2022), while also accounting for 75% of the total area equipped for irrigation, making it the most water-demanding region in terms of *IR* (Wriedt et al., 2008). However, climate change-induced temperature increases and intensified droughts have led to a reduction in available water resources in this region, particularly from snowmelt and river flows—a trend projected to worsen under future climate scenarios (Parmesan et al., 2022). At the heart of this region lies the Po River Basin in Northern Italy, a major agricultural hotspot with intensively cultivated lands that support more than 35% of Europe's agricultural production (Carlson et al., 2025). The majority of these lands are irrigated, placing the area among the top regions with the highest *IR* in Europe (Eurostat, 2019). Nonetheless, local irrigation practices are relatively inefficient (i.e., ~50%), and when combined with climate change impacts—particularly the reduction of snowmelt—and increasing water demand, put the Po River Basin under serious threat with respect to water resources (Carlson et al., 2025).

Despite the critical importance of long-term *IR* and its trends for water allocation and management at both regional and continental scales, the Po River Basin remains underrepresented in the literature in this regard. A recent effort by (Galli et al., 2025) provided crop-specific *IR* estimates at 1 km resolution across Italy using a model based on the FAO 56 single-K_c approach for 2013–2023 period, representing a valuable contribution to the growing demand for high-resolution *IR* data in Italy. However, its decade-long temporal coverage limits its applicability for long-term trend analysis, the use of a single-layer SWB constrains the physical representation of *E* partitioning and topsoil moisture dynamics, and for the Po River Basin specifically, being designed for the national scale, it relies on globally uniform crop parameters rather than region-specific ones that better capture local agronomic conditions. There remains therefore a need for *IR* estimation frameworks that are: 1. driven by long-term climate records, 2. more physically consistent in their representation of soil-plant-atmosphere interactions, 3. computationally efficient enough to operate at regional scale over long-term periods, and 4. reliant on globally available input data which make them potentially transferable to other intensively irrigated agricultural regions. To address this, the present study introduces a spatially distributed two-soil-layer SWB modeling framework (topsoil-subsoil) to estimate $ET_{c\ act}$, ET_c, and *IR*. The model is applied then to maize and forages, two major irrigated crops in the Po River Basin, to provide *IR* estimates over the period 1981–2022 at 2.2 km spatial resolution which is subsequently used to investigate long-term trends in *IR*.

The proposed framework advances beyond existing approaches applied in the Po River Basin in several interconnected ways. In terms of soil structure and moisture dynamics, rather than assuming a single homogeneous set of soil hydraulic properties for the entire soil profile, the model accounts for the vertical heterogeneity of soil hydraulic properties up to the crop root depth. In addition, infiltration from the topsoil to the root zone is explicitly simulated to improve soil moisture profile accuracy, and a modified approach to estimating the soil evaporation reduction coefficient is adopted to improve *E* estimation compared to the standard FAO 56 formulation. Regarding the soil-plant-atmosphere interactions processes, the model separates *Tr* from *E*, and interception, the fraction of precipitation retained by the vegetation canopy and never reaching the soil, is explicitly accounted for through Leaf Area Index (*LAI*) and Fraction of green vegetation Cover (*FC*) data. The explicit topsoil water balance produces soil moisture estimates in the uppermost soil layer that are physically compatible with satellite-based surface soil moisture retrievals. This structural compatibility opens a direct pathway for future reconciliation with remote sensing soil moisture retrievals, as well as their potential assimilation, offering a means to further constrain model estimates of *E* and root zone soil moisture. Finally, spatial variability in crop parameters for different regions across the basin is accounted for, reflecting local differences in crop development and canopy characteristics that are critical for a more accurate regional *IR* estimation. Despite the physical complexity of the processes represented, the framework is designed to be computationally efficient, enabling spatially distributed simulations at regional scale with high spatial resolution input data over multi-decadal periods. Together, these features make the proposed model a physically consistent, computationally efficient, parsimonious and potentially transferable framework well suited to the practical needs of regional water resource assessment and long-term irrigation planning.

2. Data

2.1. Study area

The Po River Basin, located between 44°N–47°N and 6.5°E–12.5°E, has a drainage area of 71,327 km^2, 98% of which lies in northern Italy. The basin contains extensive agricultural land supplying approximately 40% of the country's food demand (Montanari et al., 2023). The region has a humid subtropical (temperate) climate, characterized by hot summers and cool winters (Beck et al., 2018), with annual precipitation ranging from 1000 to 1200 mm (De Lannoy et al., 2024). According to the Italian National Institute of Statistics (ISTAT) latest agricultural census report (Italian National Institute of Statistics, 2021), the main crops cultivated in the Po River Basin include cereals, orchards, vine, and forages, many of which require irrigation. The majority of the agricultural lands are located in Piedmont, Lombardy, Emilia-Romagna, and Aosta valley regions which were considered in this study.

2.2. Meteorological data

ERA5 reanalysis data (Hersbach et al., 2020), developed by the European Centre for Medium-Range Weather Forecasts (ECMWF), is the most widely used georeferenced global dataset on climate variables having a spatial resolution of 0.28° (~31 km) at the equator, while its derived products—such as ERA5-Land and the regional reanalysis for the European domain (CERRA)—offer finer resolutions of 9 km and 5 km, respectively. For agricultural management applications, such as assessing crop water stress and *IR*, higher-resolution data can be transformative, as they provide greater spatial detail and improve results accuracy in regional- and basin-scale studies. In this context, the Centro Euro-Mediterraneo sui Cambiamenti Climatici (CMCC) recently published the Very High-Resolution Reanalysis for Italy (VHR-REA_IT) dataset, a dynamically downscaled version of ERA5 for Italy produced using the regional climate model COSMO-CLM (Rockel et al., 2008), with a spatial resolution of 0.02° (~2.2 km). Compared to observational and measurement data, VHR-REA_IT has shown satisfactory performance (Adinolfi et al., 2023), and was therefore used in this study as the source of all meteorological inputs.

2.3. Crop and soil properties data

In addition to meteorological data, crop parameters such as crop coefficient (K_c), root depth, and depletion fraction for root zone are essential for the modeling. Estimating $ET_{c\ act}$ following the FAO 56 method requires K_c values for the initial, middle, and late growth stages, as well as the duration of each stage, including planting and harvesting dates. To ensure the highest possible accuracy for the study area, data were sourced primarily from regional documents along with technical

reports and when no information was available, data from the Water Footprints for Nations (Chapagain and Hoekstra, 2004) and (Pereira et al., 2025) were adopted. During the initial and middle growth stages, the daily crop coefficient values remain constant while for the two transition periods of developing (ascending from end of initial stage to beginning of middle stage) and late stage (descending from end of middle stage to the harvest day) linear interpolation was used to estimate daily values (Allen et al., 1998).

When isolating *Tr* from *E* (e.g. present study), $_{Kc}$ must be adjusted to reflect only the crop characteristics to estimate *Tr*; this adjusted coefficient is known as the basal crop coefficient (K_{cb}). According to Fischer et al. (2021), the Po River Basin falls under a temperate climate classification, which corresponds to a subhumid climate within the FAO 56 framework (Berti et al., 2014). Based on this, and having K_c values, the corresponding K_{cb} values were estimated using the approach outlined in Table 18 of FAO 56 (Allen et al., 1998), where a fixed value is subtracted from K_c depending on the crop type or category.

LAI and *FC* data required for estimating interception and *E* (see Sections 3.3 and 3.4, respectively) were sourced from the Copernicus Land Monitoring Service (CLMS), which provides dekadal (i.e., 10-day recurrence) data for the period 2014–2025 (at the time this paper was written) at a spatial resolution of 300 m, based on PROBA-V and Sentinel-3/OLCI data (Copernicus Land Monitoring Service, 2017a, 2017b). *LAI* is defined as half the total surface area of the convex envelope enclosing the green canopy elements, expressed per unit of horizontal ground area. This definition captures non-flat elements such as needles and stems, resulting in a more accurate representation of vegetation structure (Verger et al., 2023). *FC* is defined as the fraction of ground surface that is covered by vegetation which is used to separate vegetation and soil which is critical for estimating interception and evaporation.

Assuming that the temporal dynamics of *LAI* and *FC* follow a pattern similar to K_{cb}, three representative values—corresponding to the initial, mid, and late growth stages—were assigned for both *LAI* and *FC* for each crop and a linear interpolation was used for the transitional periods between growth stages to estimate the daily values. To extract these representative values, the High Resolution Layer Crop Type (CTY) data for 2018–2022 (Copernicus Land Monitoring Service, 2021) from CLMS, which is a high resolution (10 m) croplands data across Europe, was used as a mask over the *LAI* and *FC* data of the median date of each growing stage. Since CTY does not provide specific crop land data on forages, EUROCROPMAP dataset (d'Andrimont et al., 2021) which is another high resolution (10 m) croplands data across Europe, was used to mask *LAI* and *FC* data for forages. Eventually, the average value of *LAI* and *FC* data corresponding to croplands in the study area representing each crop on each date was used as the representative value. It should be noted that the uncertainty associated with using this assumption was negligible according to the results of a sensitivity analysis conducted comparing the distributions of three interception scenarios over 2018–2022: (i) daily dekadal *LAI* and *FC* values, (ii) per-year monthly mean *LAI* and *FC* values, (iii) long-term monthly mean *LAI* and *FC* values, the latter corresponding to the assumption adopted in this study. The maximum difference in median interception between the daily and long-term mean scenarios across all months was 0.009 mm d^{-1} , with nearly identical interquartile ranges in all cases.

Table 1 presents the summary of main crop parameters used in the present study while table SM1 in supplementary material contains data used here for *LAI* and *FC*.

Soil physical properties, such as the percentage fractions of sand and clay, are sourced from SoilGrids v2.0 (Poggio et al., 2021), a global soil property dataset developed using a large number of soil observations. Soil hydraulic properties, including soil water content at field capacity, permanent wilting point, and saturation, are obtained from HiHydroSoil v2.0 (Simons et al., 2020), a global soil hydraulic dataset derived by applying Mualem–van Genuchten pedotransfer functions to SoilGrids v2.0 data. Both datasets provide information for six soil layers (0–5, 5–15, 15–30, 30–60, 60–100, 100–200 cm) at a spatial resolution of 250 m, and were therefore resampled to match the spatial resolution of the meteorological data.

3. Methods

3.1. Modeling framework

We developed a daily time-step SWB model, named **AGRHYD** (AGRiculture HYDrology), built on the works done by (Rolle et al., 2022, 2021; Tuninetti et al., 2015). The model follows the FAO 56 dual-K_c approach to estimate $ET_{c\ act}$, ET_c and, consequently, *IR* at point and grid

Table 1
Crop properties used in the present study. *Kc* is crop coefficient, *Kcb* is crop basal coefficient, each given at the initial, middle-, and late-season growth stages. For perennial crops, for dual-K_c approach, the *kcb* is set to 0.15 before Greenup and after harvest while for single-K_c approach, the season is considered only between the Greenup and harvest. *R1* and *R2* are the rooting depths (m) for irrigated and rainfed conditions, respectively. *DF* is the soil water depletion fraction in the root zone. *SS* and *SE* are the start of the season and end of the season dates, respectively. According to ISTAT, forages constitutes permanent and temporary pasture, maize for silage, alfalfa, and combination of them across the regions and therefore *Kc* and *Kcb* for forages vary across the regions within the specified ranges.

Crop		Kc/Kcb initial	Kc/Kcb Middle	Kc/Kcb late	R1	R2	DF	SS	SE
Wheat	-	0.68/ 0.15	0.96/ 0.84	0.38/ 0.34	1	1.5	0.55	15 Nov	14 July
Vine	-	0.48/ 0.15	0.68/ 0.63	0.59/ 0.54	2		0.35	**Perennial**	
								Greenup	**Harvest**
								1 Apr	15 Sep
Maize	-	0.33/ 0.15	1/ 0.95	0.4/ 0.35	0.8	1.2	0.5	1 Apr	20 Aug
Forages	Permanent pasture	0.7/ 0.65	0.89/ 0.84	0.75/ 0.7	0.5	1.5	0.6	**Perennial**	
								Greenup	**Harvest**
								15 Mar-8 Apr	15 Sep-27 Oct
	alfalfa	0.5/ 0.45	1/ 0.95	1/ 0.95	2		0.55	**Perennial**	
								Greenup	**Harvest**
								15 Mar	10 Oct
	Permanent pasture, alfalfa	0.6/ 0.55	0.95/ 0.9	0.88/ 0.84	1.5		0.6	**Perennial**	
								Greenup	**Harvest**
								15 Mar	15 Sep
	Maize for silage, alfalfa	0.4/ 0.35	1/ 0.95	0.95/ 0.9	1	1.7	0.5	1 Apr	15 Aug
	Maize for silage	0.3/ 0.15	1/ 0.95	0.89/ 0.84	1	1.7	0.5	1 Apr	15 Aug

scales, based on soil properties, crop phenology, and meteorological data for seasonal and perennial crops under rainfed and irrigated regimes. Two soil compartments, namely topsoil and subsoil are considered from which *E* and *Tr* are estimated, respectively where summed up $ET_{c\ act}$ is obtained. Fig. 1 represents AGRHYD workflow.

3.2. Reference evapotranspiration estimation

FAO P-M equation is recommended by FAO 56 for estimating daily reference crop evapotranspiration (ET_o), and is expressed as:

$$ET_{0,i} = \frac{0.408\ \Delta\ (R_{n,i} - G_i)\ +\ \gamma \frac{900}{T_{mean,i}+273}\ u_{2,i}(e_{s,i} - e_{a,i})}{\Delta\ +\ \gamma(1 + 0.34\ \ u_{2,i})} \quad (1)$$

Where R_n is the net radiation at top of canopy [MJ m^{-2} day^{-1}] on day *i*, *G* is soil heat flux density [MJ m^{-2} day^{-1}] on day *i*, $T_{mean,i}$ is mean air temperature at 2 m height [°C] on day *i*,u_2 is wind speed at 2 m height on day *i* [m s^{-1}],e_s is saturation vapour pressure [kPa] on day *i*,e_a is actual vapour pressure deficit [kPa] on day *i*, Δ is slope vapour pressure curve [kPa $°C^{-1}$],γ is psychrometric constant [kPa $°C^{-1}$].

When all required inputs for the FAO P-M equation are not available or associated with high uncertainty, the Hargreaves-Samani (H-S) equation can be used as an alternative as recommended by FAO 56 and is expressed as:

$$ET_{0,i} = K_{HS}\ (T_{mean,i} + 17.8)(T_{\max,i} - T_{\min,i})^{0.5} R_{a,i} \quad (2)$$

Where K_{HS} is an empirical coefficient equal to 0.0023, $T_{mean,i}$, $T_{\max,i}$, $T_{\min,i}$ are the mean, maximum and minimum temperature on degrees of Celsius [°C] on day *i*. $R_{a,i}$ is the equivalent evaporation [mm] on day *i* which is obtained by dividing extraterrestrial solar radiation [MJ m^{-2}] on day *i* by the latent heat of vaporisation. All the variables required for (1) and (2) are either directly provided by VHR-REA_IT or derived using the relationships described by (Allen et al., 1998) incorporating VHR-REA_IT data. We estimated ET_o using both methods above to compare and assess their impact on $ET_{c\ act}$ estimates.

3.3. Interception

Precipitation intercepted by vegetation does not reach the soil and hence not contributing to the SWB. Following Braden (1985); Von-Hoyningen-Huene, (1983) and incorporating *LAI* and *FC*, the intercepted precipitation of day *i* is estimated as:

$$INT_i = 0.2\ LAI_i\ \left(1 - \frac{1}{1 + \frac{FC_i\ P_i}{0.2\ \ LAI_i}}\right) \quad (3)$$

Where P_i is total precipitation [mm] on day *i*.

INT is assumed to evaporate directly from the leaf surface, which slightly alters the vapor pressure deficit above the canopy and reduces the atmospheric evaporative demand. To account for this effect, *INT* is subtracted from ET_o in the model and the remainder enters the SWB cycle as ET_o.

3.4. Soil-water balance in topsoil

The daily SWB in the topsoil (0–5 cm) is used to estimate topsoil

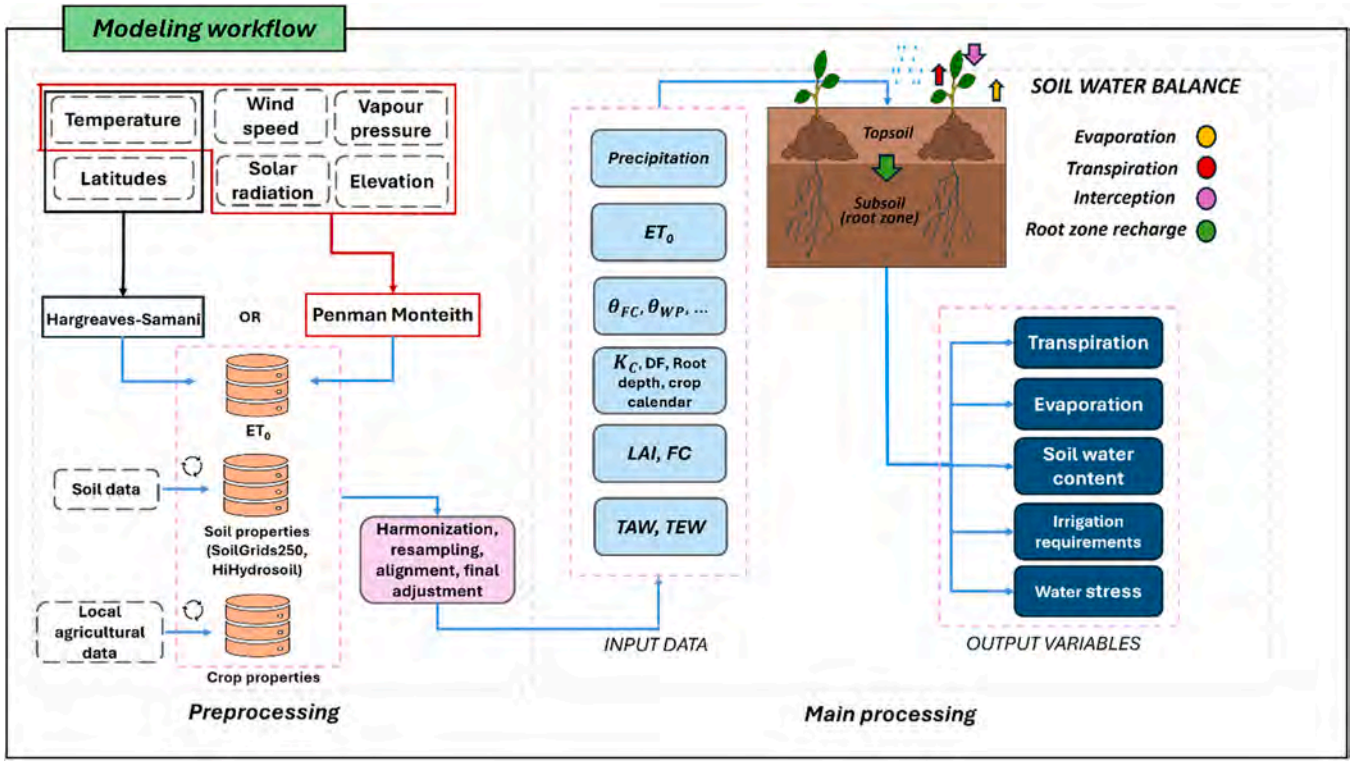


Fig. 1. Schematic overview of the AGRHYD modeling workflow. Input meteorological data include temperature and latitudinal information required for ET_o estimation using the Hargreaves-Samani (H-S) method while wind speed, relative humidity, solar radiation, and elevation (red-bordered box) can be provided to compute ET_o using the FAO 56 Penman-Monteith (P-M) method. Along with meteorological forcing, soil hydraulic properties and local agricultural data are harmonized, resampled, and spatially aligned prior to model execution. The model core integrates meteorological forcing (precipitation and ET_o), soil hydraulic parameters (field capacity θ_{FC}, wilting point θ_{WP}), crop parameters (crop coefficients K_c, K_{cb}, depletion fraction DF, root depth, crop calendar, leaf area index *LAI*, and fraction of green vegetation cover *FC*), and derived soil water storage parameters (total available water *TAW* and total evaporable water *TEW*). The two-compartment soil structure (top right) distinguishes between a topsoil evaporation layer and a subsoil root zone layer, with separate water balance computations for each compartment. Model outputs include crop transpiration, soil evaporation, soil water content, irrigation requirements, and the water stress coefficient, produced at daily time steps.

moisture and hence E and infiltration into the subsoil. The 5 cm depth was deliberately chosen to be physically compatible with satellite-based surface soil moisture retrievals, which are typically sensitive to the uppermost 2–5 cm of the soil profile, thereby facilitating future reconciliation and potential assimilation of the modeled topsoil moisture with remote sensing observations. The soil properties for the first layer of the soil data is directly used for the topsoil. The total daily precipitation—subtracting interception—is considered as the water input which combined with the soil moisture in the topsoil profile, supplies the water demand for daily E . When the topsoil water content exceeds that of field capacity, it is assumed that the excessive water is infiltrated downward into the subsoil which is defined as root zone recharge. The topsoil SWB is expressed as:

$$D_{tp,i} = D_{tp,i-1} - (P - INT - R)_i - CR_i + R_{rz,i} + E_i \quad (4)$$

Where $D_{tp,i}$ and $D_{tp,i-1}$ are the water deficit in the topsoil at the end of the day i and at the end of day i-1 (i.e., beginning of the day i), respectively, P_i is the total effective precipitation depth on day i, R_i is surface runoff on day i, CR_i is the capillary rise from a saturated lower soil layer or groundwater table on day i, $R_{rz,i}$ is root zone recharge on day i, E_i is soil evaporation on day i. All variables are expressed in mm.

The capillary rise contribution is assumed negligible in this study according to (Mialyk et al., 2024)and also as the water table is assumed to be out of reach for the roots in line with previous studies adopting the same approach (Galli et al., 2025; Tuninetti et al., 2015; Wang et al., 2023). Additionally, agricultural fields in the study area, being mostly in the basin lowlands, are considered to have negligible slope. Therefore, surface runoff is assumed to be negligible which is a sound assumption consistent with studies conducted under comparable conditions (Olivera-Guerra et al., 2023). In cases where the fields are inundated and the soil profile water content exceeds that of field capacity, it is assumed that drainage occurs rapidly enough to redistribute excess water downward into the subsoil (i.e., root zone recharge) leaving the soil profile at field capacity.

The water deficit in the topsoil is determined relative to the Total Evaporable Water (*TEW*), which is maximum water depth in mm that can be evaporated from the topsoil. *TEW* is expressed as:

$$TEW = 1000(\theta_{fc} - \ 0.5\ \theta_{wp})Z_e \quad (5)$$

Where θ_{fc} and θ_{wp} represent volumetric soil water content [m^3/m^3] at field capacity and the permanent wilting point, respectively in the topsoil, and Z_e is the topsoil depth in m. The initial value for $D_{tp,i-1}$ to run the simulation is assumed as 50% of the *TEW*.

Soil evaporation on day i (E_i) is estimated as:

$$E_i = K_{e,i}ET_{0,i} = \min(K_{r,i}(K_{c\ \max} - \ K_{cb,i}), f_{ew,i}\ K_{c\ \max})ET_{0,i} \quad (6)$$

Where $K_{e,i}$ is soil evaporation coefficient on day i which describes E component of $ET_{c\ act}$, $K_{r,i}$ is the non-dimensional evaporation reduction coefficient on day i, K_{cmax} is the maximum crop coefficient, $K_{cb,i}$ is crop basal coefficient on day i, and $f_{ew,i}$ is the exposed and wetted soil fraction from which the most evaporation occurs on day i.

K_r modulates E through two stages: the energy-limited stage and the falling-rate stage, ranging from 1 to 0. In the energy limited stage, the soil surface is sufficiently wet, and E occurs at its potential rate, constrained only by the available energy ($K_r = 1$). (Merlin et al., 2011) demonstrated that E rate exhibits a nonlinear relationship with surface soil moisture (unlike the original relationship suggested by FAO 56 which is linear), and that K_r can be estimated primarily using soil texture information. This approach has been recently adopted in studies implementing the FAO 56 dual-K_c approach (Amazirh et al., 2021; Olivera-Guerra et al., 2023)

in which K_r is expressed as:

$$K_{r,i} = \left[0.5 - 0.5\ \cos\left(\frac{\pi\ \theta_{tp,i}}{\theta_{SAT,tp}}\right)\right]^{\alpha} \quad (7)$$

Where $\theta_{tp,i}$ is the actual soil moisture in the topsoil on day i which is determined as $TEW - D_{tp,i}$, $\theta_{SAT,tp}$ is the soil moisture at saturation in the topsoil, and α is a semi-empirical parameter that depends on both the depth of the soil moisture measurement and soil texture. For further details on the estimation of α refer to (Amazirh et al., 2021).

K_{cmax} in Eq. (6) represents the upper limit of the combined Tr and E potential, acknowledging that $ET_{c\ act}$ is constrained by the available energy. In this study, K_{cmax} is assumed to be equal to the crop coefficient (i.e., K_c) corresponding to middle growth stage which gives the upper limit of $ET_{c\ act}$.

In Eq. (6) f_{ew} is obtained using *FC* and when wetting occurs solely due to precipitation, as in this study, and it is expressed as:

$$f_{ew_i} = 1 - FC_i \quad (8)$$

3.5. Soil-water balance in subsoil

To estimate daily Tr, the SWB in the subsoil is employed to determine the soil moisture state in this compartment. Soil hydraulic properties proportional to the root depth is obtained by taking a weighted average across the soil data layers below the topsoil level up to the root depth. The soil moisture in this compartment is assessed based on the water deficit in the subsoil and the recharge flow from the topsoil (i.e., R_{rz}). The SWB in subsoil is expressed as:

$$D_{sb,i} = D_{sb,i-1} - R_{rz,i} + Tr_i + DP_i \quad (9)$$

Where $D_{sb,i}$, and $D_{sb,i-1}$ are the water deficits in the subsoil at the end of the day i and i-1, respectively, Tr is the crop transpiration on day i, and DP_i is the deep percolation on day i. All variables are expressed in mm.

The water deficit in the subsoil is determined relative to the Total Available Water (*TAW*), which represents the amount of water between the volumetric soil water content at field capacity and at permanent wilting point available for plant to uptake for Tr relative to the root depth. *TAW* is expressed as:

$$TAW_i = 1000(\theta_{fc} - \theta_{wp})RD_i \quad (10)$$

Where RD_i is the crop root depth in m on day i. The initial value for $D_{sb,i-1}$ to run the simulation is assumed as 50% of *TAW*.

Tr is expressed as:

$$Tr_i = K_{s,i}\ K_{cb,i}\ ET_{0,i} \quad (11)$$

where $K_{s,i}$ is the water stress coefficient on day i, and $K_{cb,i}$ is basal crop coefficient on day i.

K_s is determined based on the subsoil moisture status and is expressed as:

$$K_{s,i} = \frac{TAW - \ D_{sb,i-1}}{TAW - RAW} \quad (12)$$

Where *RAW* is the readily available water, which is the amount of water that can be easily extracted from the soil matrix by plant roots. *RAW* also represents a threshold for the subsoil water deficit where as long as the deficit is below this threshold, water is transported sufficiently fast from the soil to the plant to fully meet transpiration demand thus no water stress ($K_s = 1$). When water deficit exceeds this threshold (i.e., soil moisture is below *RAW*), water extraction from the soil becomes more difficult due to stronger adhesion between water molecules and soil particles, leading to decrease in K_s and water stress ($0 \leq K_s < 1$). *RAW* is estimated as:

$$RAW_i = TAW_i \cdot DF \quad (13)$$

Where *DF* is a dimensionless factor ranging from 0 to 1 and represents the fraction of *TAW* that can be depleted from the root zone before the onset of water stress and varies between crops.

Eventually, summing Tr_i and E_i, daily $ET_{c\ act}$ reads:

$$ET_{c\ act\ i} = Tr_i + E_i \quad (14)$$

Another simulation was performed employing the FAO 56 single-K_c method with interception in order to compare the results between the two approaches. To this end, the procedure similar to that of the subsoil was followed though for a single soil profile. A weighted average of soil hydraulic properties was computed to obtain a single representative value for each property for the soil profile. For more detail on FAO 56 single crop coefficient method refer to (Rolle et al., 2022, 2021).

3.6. Estimation of irrigation requirements

IR is the minimum amount of water needed, in addition to precipitation, to meet crop water demand to maintain optimal growth without water stress (i.e., maximum *Tr*). In these conditions (i.e., irrigated) K_s is set to 1 to estimate maximum *Tr* in Eq. (11). Whenever the water deficit in the subsoil exceeds the *RAW*, irrigation is applied to replenish the deficit in the subsoil. This irrigation water should represent the minimum amount expressed in mm required to offset the water deficit in the topsoil, and subsequently in the subsoil to be applied to theoretically avoid water stress in plants.

$$IR_i = D_{sb,i} - RAW_i + D_{ts,i} \quad \text{for } D_{sb,i} > RAW \quad (15)$$

It should be noted that the *IR* estimated here represent net irrigation requirements and do not account for conveyance losses or field application efficiency. As such, they characterise the crop irrigation water demand driven by climate and crop phenology independent of the irrigation methods or infrastructure.

In order to properly map the estimated *IR* for each crop, crop-specific irrigated surface area maps are necessary. The latest Italian National Institute of Statistics (ISTAT) agricultural census provides irrigated areas of cultivated crops at the municipal level for year 2020. The reported irrigated area for each crop and municipality was then proportionally redistributed across the 2.2×2.2 km grid using irrigation channel network data where agricultural parcels within each municipality were ranked by their proximity to irrigation channels and irrigated areas were assigned iteratively starting from parcels adjacent to the irrigation channels and progressively extending outward until the allocated irrigated area matched the ISTAT municipal totals. To guarantee internal consistency, a constraint was imposed at the grid-cell level such that the sum of irrigated areas across both crops did not exceed the physical area of a cell. In cases where proportional allocation exceeded this limit, irrigated areas of both crops (i.e., maize and forages) within the affected cell were rescaled proportionally to maintain their relative distribution while respecting the maximum cell capacity. To ensure the validity of using a single-year irrigated area map as representative of crop spatial distribution over the simulation period, a change detection analysis of maize and forages crop shares was conducted for the period 1990–2018 using the crop-type dataset provided by (Baumert et al., 2024). The analysis revealed consistently low variation in the spatial distribution of both crops across the Po River Basin. Moreover, since both maize and forages in the study area are predominantly irrigated crops, the observed stability in their spatial distribution implies that changes in irrigated area over the simulation period can be considered negligible. These factors together support the assumption that a static irrigated area map derived from the 2020 is valid and representative over the *IR* simulation period.

3.7. Model evaluation through datasets intercomparison

IR is a theoretical construct that cannot be directly monitored; hence, no field data are available to be used for its evaluation. However, the key variable for estimating *IR* is ET_c which represents the upper bound for $ET_{c\ act}$. An accurate estimate of $ET_{c\ act}$ implies that modeling framework used for ET_c is also sound, thereby underpinning the reliability of *IR* estimates and, consequently, the model's performance. Therefore, we evaluated the model's $ET_{c\ act}$ output as a proxy for *IR* estimates accuracy. Due to the lack of field-based $ET_{c\ act}$ measurements in the study area, state-of-the-art satellite-derived land evapotranspiration products from the GLEAM v4.2a and WaPOR v3 datasets were used as reference to evaluate the AGRHYD $ET_{c\ act}$ estimates, and by extension, the estimated *IR*.

GLEAM provides daily estimates of *E* and *Tr* at a spatial resolution of ~11 km, which were summed to obtain daily $ET_{c\ act}$. WaPOR offers dekadal (i.e., 10-day) data on actual evapotranspiration and interception (*AETI*), along with interception (*I*) component, at a spatial resolution of 300 m. For WaPOR, $ET_{c\ act}$ was derived by subtracting *I* from *AETI*, and the resulting data were linearly interpolated to obtain daily values hereafter referred to as WaPOR $ET_{c\ act}$. Unlike AGRHYD, both WaPOR and GLEAM account for irrigation water inputs in their $ET_{c\ act}$ estimates, WaPOR by solving the P-M equation for the canopy incorporating earth observation data, and GLEAM by assimilating satellite soil moisture data. To ensure a fair comparison, we therefore selected wheat and vine, two predominantly rainfed crops in the study area, in which irrigation water is not typically included in $ET_{c\ act}$ estimates. Finally, since WaPOR v3 is available from 2018 onward, the evaluation period was restricted to 2018–2022 for all three datasets (WaPOR, GLEAM, and AGRHYD).

The three datasets differ in spatial resolution: WaPOR at 300 m, AGRHYD at 2.2 km, and GLEAM at ~11 km. Downscaling coarse data (i.e., GLEAM) is associated with uncertainties and we preferred not to modify the original resolution of WaPOR or GLEAM. Instead, one dataset with coarser grid was considered as reference and $ET_{c\ act}$ values from finer-resolution data were aggregated to match the coarser reference grid using spatial averaging. Another challenge was finding areas across the reference grid where wheat and vine constitutes either a monoculture or a dominant land cover fraction of the pixel, so that $ET_{c\ act}$ values are primarily attributable to the target crop. Using the GLEAM grid as reference, three pixels dominated by vine and two by wheat were identified. Unlike vine, wheat fields are rather fragmented across the study area, which limited the chance for finding more GLEAM-scale reference pixels dominated by wheat fields. To this end, AGRHYD grid was used as the reference, yielding six more reference pixels with relatively high share of wheat fields. Reference pixels were identified using the Copernicus crop type maps for each year from 2018 to 2022. In two of the wheat reference pixels, insufficient wheat fields coverage was identified in certain years and therefore, those years were excluded from the comparison. For datasets with finer resolution than the chosen reference pixels, only the pixels largely overlapping with wheat or vine parcels were selected. This ensures that the extracted $ET_{c\ act}$ values are largely attributable to the target crops rather than mixed land cover (Figs. 2 and 3).

4. Results and discussions

In this section, in the first part we will show the results on comparison between $ET_{c\ act}$ estimated by the model and those of the WaPOR and GLEAM and discuss the effect of P-M and H-S methods on estimated ET_0. This is followed by the comparison between the single- and dual-K_c approaches and the monthly $ET_{c\ act}$ comparisons between the three datasets. Then in the second part, we provide the results on *IR* and its trends analysis and contribution of climate drivers in the *IR* trend.

4.1. Evapotranspiration estimates and model performance

The model was run to estimate $ET_{c\ act}$ for both the single and dual Kc approaches, using ET_0 derived from the FAO P-M and Hargreaves–Samani (H-S) methods for wheat and vine at selected areas. Estimated $ET_{c\ act}$ was evaluated against WaPOR and GLEAM through scatter plot analysis, using Pearson's correlation coefficient (*r*), the coefficient of determination (R^2), and the root mean square error (*RMSE*), as performance metrics with satisfactory results.

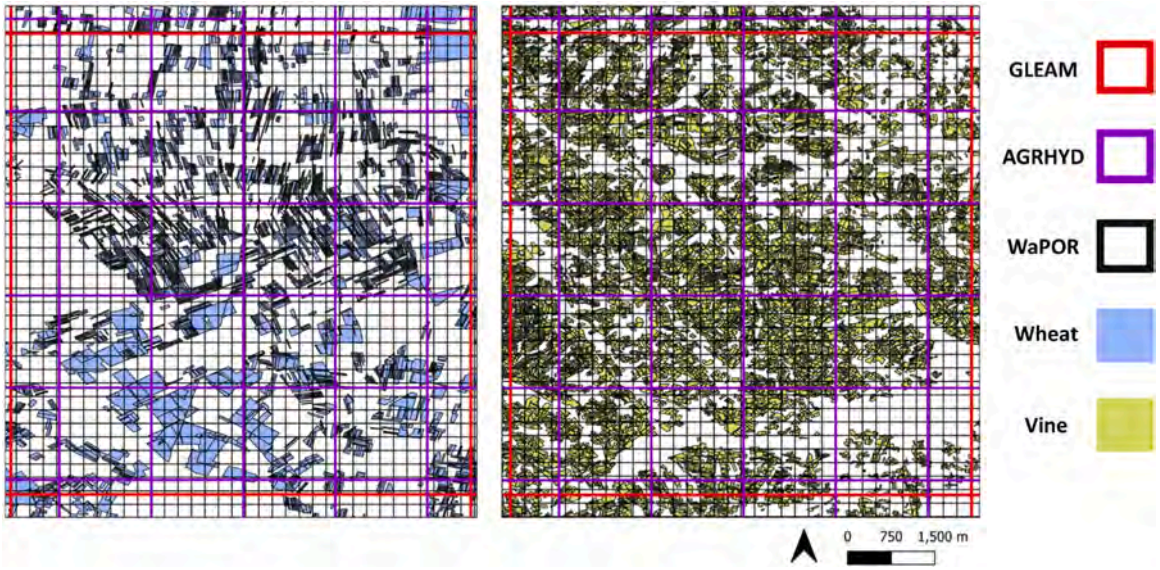


Fig. 2. Spatial distribution of wheat and vine fields in two representative reference pixels (W1 and V1 in Fig. 3) and the grids alignment for $ET_{c\ act}$ evaluation in the study area. Wheat fields are demonstrated in blue and vine fields in green. White areas represent other crops or vegetation cover.

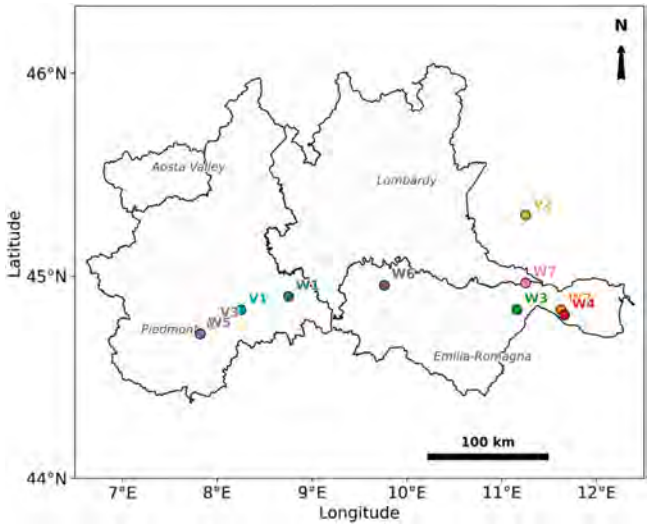


Fig. 3. Location of the reference pixels used for the evaluation of AGRHYD model $ET_{c\ act}$ estimates against WaPOR and GLEAM within the Po River Basin. Wheat locations (W1–W7) and vine locations (V1–V3) are shown as filled circles.

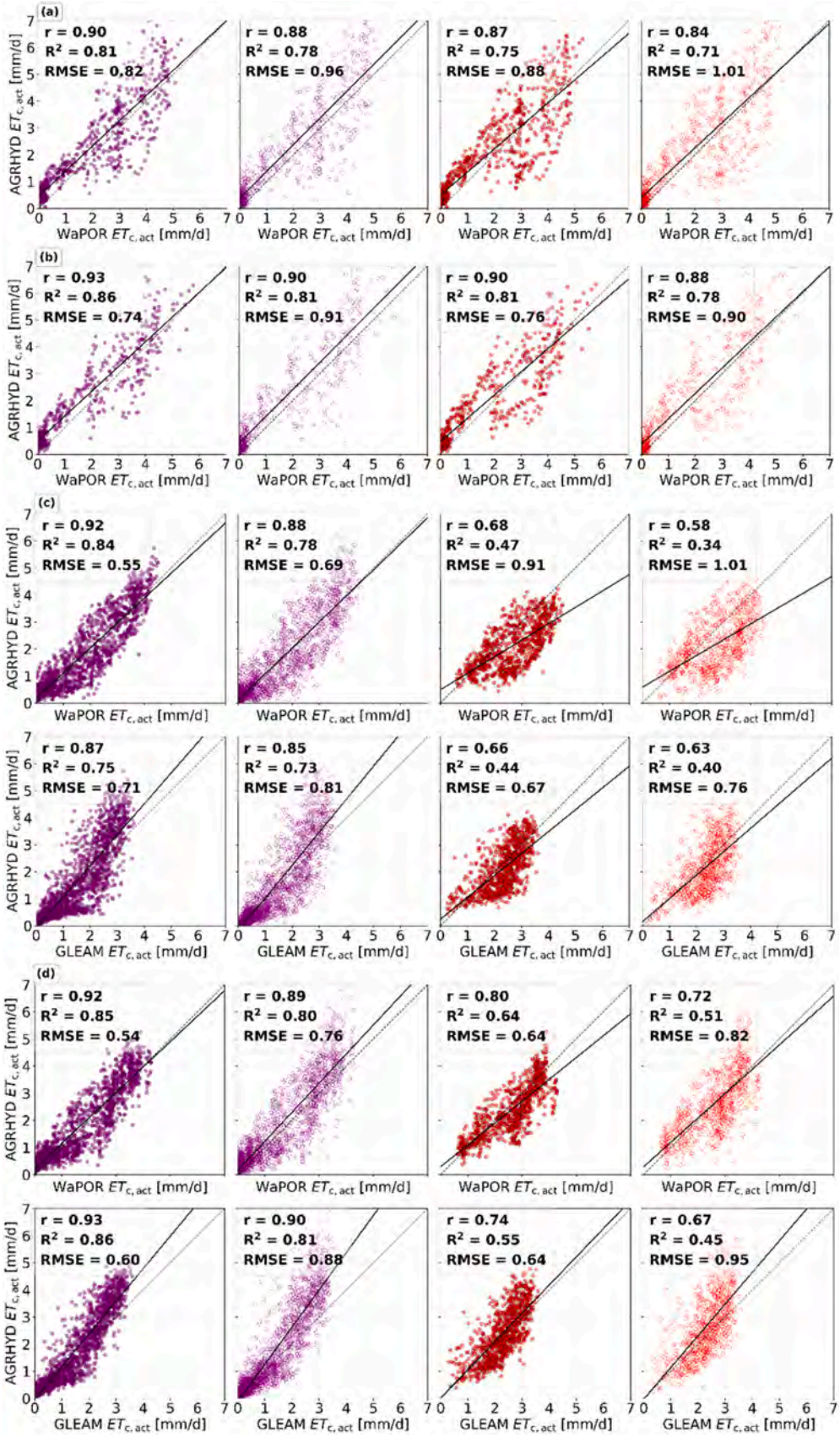
4.1.1. Effects of reference evapotranspiration method on actual evapotranspiration estimates

$ET_{c\ act}$ derived from HS-based ET_o predominantly outperformed that derived from P-M-based ET_o for both crops and under both single- and dual-Kc approaches, when compared against both WaPOR and GLEAM datasets, with average $r = 0.83$ and RMSE $= 0.86$ mm day^{-1} for H-S-based ET_o, compared to $r = 0.79$ and RMSE $= 1$ mm day^{-1} for P-M-based ET_o. This corresponds to around an average of 4% higher correlation coefficient and a 18% lower RMSE when using HS-based ET_o. (Fig. 4 presents the results for four representative reference pixels while the results for other reference pixels are shown in fig. SM1 in supplementary material.)

This difference likely reflects the quality and representativeness of the reanalysis data inputs used to estimate the P-M based ET_o. The P-M formulation requires a broader set of variables, some of which are associated with considerable uncertainty in reanalysis datasets. In particular, dew point temperature, needed to estimate actual vapour pressure, and wind speed are notoriously difficult to represent accurately over agricultural fields and above the canopy. These uncertainties likely propagate into the P-M-based ET_o estimates, partially explaining the weaker agreement with the reference data. In contrast, the H-S method relies only on temperature and extraterrestrial radiation, which are generally measured or estimated with higher reliability. Moreover, the subhumid Mediterranean climate conditions of the study area, where solar radiation and wind regimes are relatively stable, allow H-S equation, with its reduced input requirements, to provide reliable ET_o estimates outperforming the P-M method here. Therefore, for the remainder of the study, only $ET_{c\ act}$ estimated using H-S-based ET_o was retained.

4.1.2. Comparison of Single and Dual crop coefficient approaches

Regarding the crop coefficient methods, $ET_{c\ act}$ estimated using both the single- and dual-K_c approaches presented in this study showed reasonable agreement with WaPOR and GLEAM for both crops, with the dual-K_c approach consistently outperforming the single-K_c across both crops and both reference datasets for all reference pixels (Fig. 4 and fig. SM1). For wheat, dual-K_c achieved the best performance against both WaPOR ($r = 0.88$, RMSE=0.92 mm day^{-1}) and GLEAM ($r = 0.83$, RMSE=1.02 mm day^{-1}), compared to single-K_c ($r = 0.83$, RMSE=0.98 mm day^{-1} against WaPOR and $r = 0.78$, RMSE=1.04 mm day^{-1} against GLEAM). For vine, the superiority of the dual-K_c approach was more pronounced ($r = 0.91$ and RMSE=0.58 mm day^{-1} against WaPOR and $r = 0.88$ and RMSE=0.68 mm day^{-1} against GLEAM) compared to single-K_c ($r = 0.70$, RMSE=0.86 mm day^{-1} against WaPOR and $r = 0.69$, RMSE=0.67 mm day^{-1} against GLEAM). These results confirmed the modelling framework presented here (i.e., dual-K_c approach) as the better performing configuration and further justify its adoption for the remainder of this study. Beyond performance, the presented dual-K_c framework offers methodological advantages: the explicit separation of Tr and E allows for more physically consistent simulation of soil moisture dynamics and crop water use, which is essential for subsequent analyses. This choice also aligns with recent trends in the literature, where the dual-K_c approach has become the dominant method due to its improved process representation. Therefore, all subsequent results and analyses utilise the presented dual-K_c method with ET_o derived from the H-S method, consistent with the findings of the previous section.



(caption on next page)

Fig. 4. Scatter plots showing daily $ET_{c\ act}$ (mm day^{-1}) estimates from AGRHYD model against WaPOR and GLEAM datasets for wheat and vine during the 2018-2022 growing seasons: (a)-(b) wheat reference pixels W2, W4, (c)-(d) vine reference pixels V1 and V2. Purple color indicates cases with dual-K_c approach and red color indicates cases with single-K_c approach. Filled circles represent $ET_{c\ act}$ estimates employing Hargreaves-Samani (H-S) reference ET_o while hollow circles represent $ET_{c\ act}$ estimates employing Penman-Monteith (P-M) reference ET_o. Metrics shown are Pearson's correlation coefficient (r), coefficient of determination (R^2), root mean square error (RMSE).The dashed line is the 1:1 line and the solid line is the linear regression.

4.1.3. Model's performance in different stages of growing season

The stronger agreement observed for vine compared to wheat for some reference pixels (Fig. SM1) can be attributed to two factors. First, as explained in Section 3.7, wheat fields are fragmented across the study area making it difficult to identify reference pixels composed purely of wheat and since neither WaPOR nor GLEAM are crop-specific products, the presence of other crops or vegetation within the same pixel may contribute to the observed discrepancy (Fig. 2). Second, unlike perennial vine, wheat is an annual crop with distinct planting and harvesting periods that introduce additional complexity within the FAO 56 framework. Specifically, AGRHYD applies a fixed crop calendar in which the crop coefficient curve begins to decline on a fixed date marking the onset of late-season stage, forcing $ET_{c\ act}$ to decrease toward the end of the growing season consistently across all years. In contrast, WaPOR and GLEAM implicitly capture dynamic growing seasons through their satellite-based frameworks. Consequently, even small differences in the growing season length in the reference pixel across different datasets, whether arising from interannual variability in the wheat growing season itself or from the presence of other annual crops with different phenological cycles within the same pixel, can introduce significant discrepancies when comparing $ET_{c\ act}$ estimates.

This phenomenon is clearly illustrated in Fig. 5 where in reference pixel W1, as a representative, AGRHYD $ET_{c\ act}$ estimates declined following the FAO 56 late-season reduction after 15 June (indicated by red vertical lines), while WaPOR and GLEAM $ET_{c\ act}$ values continue to increase in most years. This pattern was also observed across the other wheat reference pixels exhibiting high dispersion in the scatter plots (fig. SM2).

To understand whether the dispersion observed in the wheat scatter plots is significantly driven by this phenological mismatch, $ET_{c\ act}$ values from 16 June onwards, corresponding to the late-season stage, were masked for all three datasets for the four wheat reference pixels (W1, W3, W5, W6) where scatter plots showed the most dispersed data, mainly characterized by a distinct cluster of points with high WaPOR/GLEAM values (>3 mm day^{-1}) but low AGRHYD values (<2.5 mm day^{-1}). The histogram of data confirmed that a large number of points in these clusters belong to the post-15 June period. Specifically, on average 50% of AGRHYD $ET_{c\ act}$ values fell below 2.5 mm day^{-1} while 95% of WaPOR data and 86% of GLEAM data exceeded 3 mm day^{-1} across the four reference pixels and during the identified mismatch years. Filtering this period significantly improved the statistical metrics for wheat when compared with both WaPOR and GLEAM over the growing season up to the late-season stage. On average r increased from 0.85 to 0.90, R^2 increased from 0.72 to 0.82, and RMSE decreased from 0.97 to 0.89 mm day^{-1} across the four reference pixels (Fig. 6).

It should be noted that, however, the metrics for masked data in Fig. 6 should be interpreted as representative of model performance up to 15 June (i.e., excluding the late-season stage) for wheat in the presented reference pixels, while the metrics for all data reflect the full comparison over the entire growing season including the phenological mismatch in the late-season stage. The analyses performed here highlighted that the late-season behaviour varied across locations and years for wheat. In cases where all three datasets showed a consistent $ET_{c\ act}$ decline after 15 June, the fixed Kc curve appeared to reasonably represent the seasonal dynamics. However, cases in which WaPOR and GLEAM maintained high $ET_{c\ act}$ values beyond this date while AGRHYD declined following the fixed decreasing Kc curve, may indicate the limitation of a static crop coefficient curve in capturing actual field conditions. This limitation, however, holds under the condition that the reference pixel is predominantly covered by wheat fields and they have not yet entered the late-season stage under actual field conditions. On the contrary, where uncertainty in the applied crop calendar is low and wheat can be confidently assumed to be in the late-season stage, the primary reason behind the mismatch between the model and reference datasets is the contribution of crops or vegetation other than wheat present in the reference pixel to the WaPOR and GLEAM $ET_{c\ act}$ values which could maintain relatively high $ET_{c\ act}$ values beyond the wheat late-season stage period. In the present study, the latter explanation is more likely, both because the reference pixels for wheat mostly contained other crops or vegetation in addition to wheat, and because the crop calendar used for wheat was from the local information, reducing the uncertainty in the applied phenological timing.

Beyond the phenological mismatch, examination of the wheat $ET_{c\ act}$ time series (Fig. 5 and fig. SM2) revealed that in some years AGRHYD tended to overestimate wheat $ET_{c\ act}$, particularly during the mid-season period (May-June). This overestimation can be attributed to fundamental methodological differences among the datasets. Both WaPOR and GLEAM explicitly incorporate additional factors affecting $ET_{c\ act}$ (e.g., aerodynamic resistance, vegetation height, vapor pressure deficit), whereas in AGRHYD soil moisture availability serves as the primary limiting factor through the SWB formulation. WaPOR estimates E and Tr by directly solving the P–M equation and, unlike AGRHYD, does not employ an explicit SWB model. Instead, soil conditions are inferred using a trapezoidal relationship between vegetation cover and land surface temperature. GLEAM, while conceptually closer to AGRHYD in its use of water balance principles, assimilates microwave soil moisture data together with vegetation optical depth and atmospheric carbon dioxide to estimate E and Tr separately. Consequently, both WaPOR and

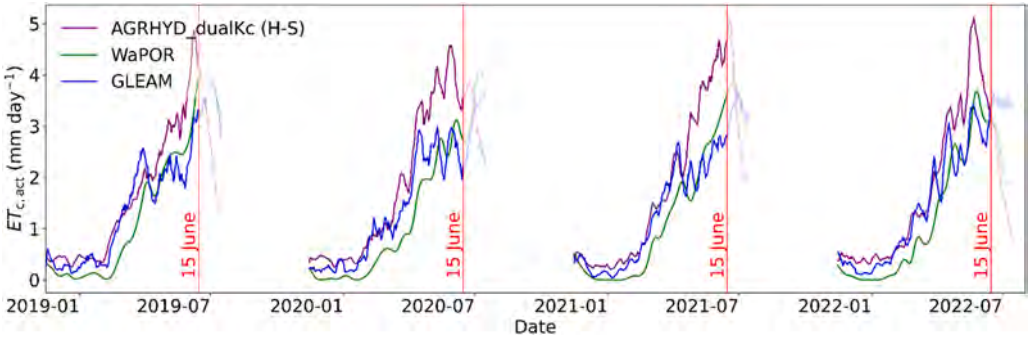


Fig. 5. Time series of 10-day moving average $ET_{c\ act}$ for wheat in reference pixel W1 from AGRHYD, WaPOR, and GLEAM during 2018–2022. Red vertical lines indicate June 15 of each year, marking the onset of the late-season stage.

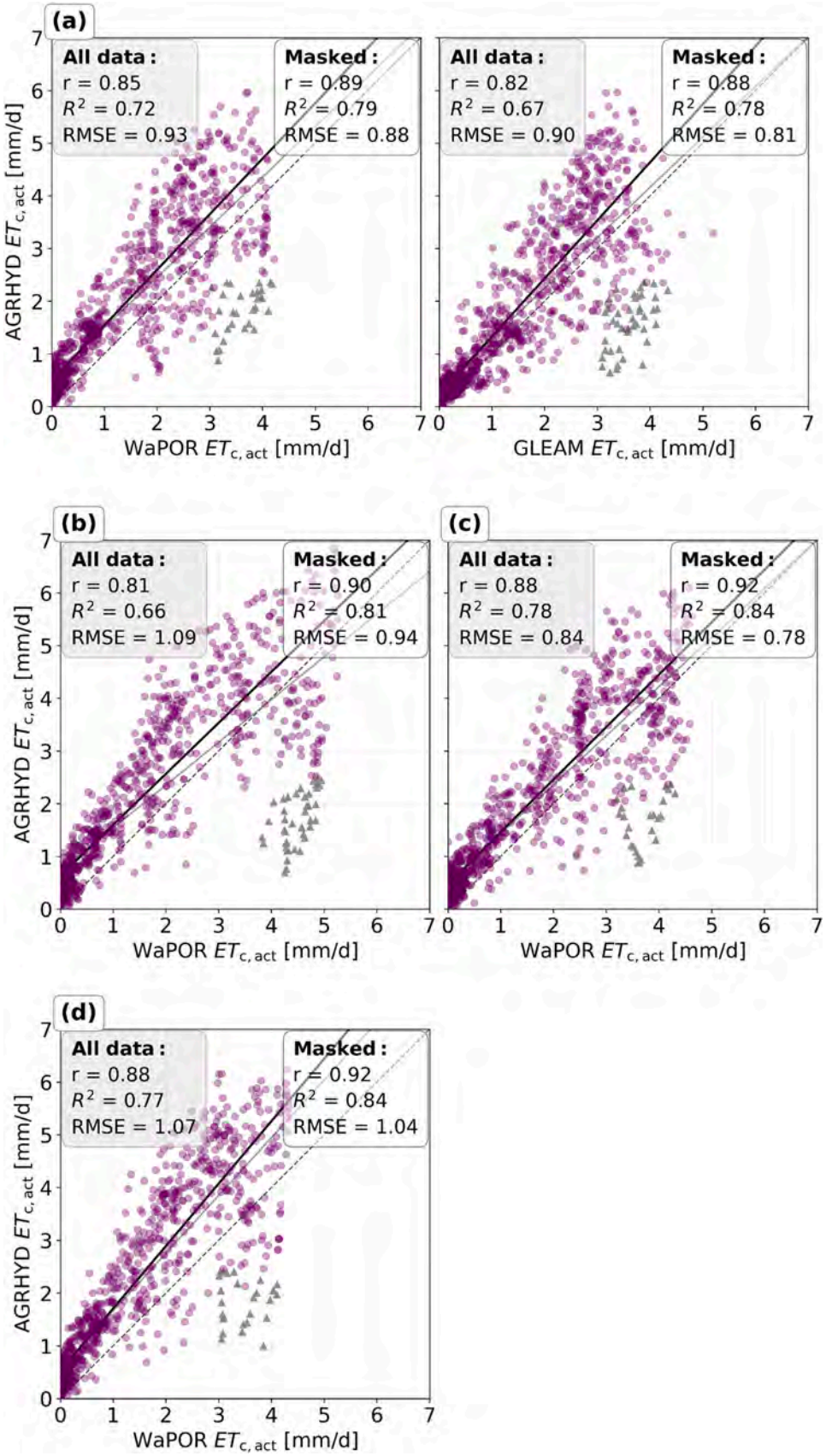


Fig. 6. Scatter plots showing daily $ET_{c\ act}$ (mm day^{-1}) estimates from AGRHYD model against WaPOR and GLEAM datasets for wheat (a) reference pixel W1, (b-d) reference pixels W3, W5, and W6 for 2018–2022. The grey triangles represents data for post-15 June. Statistical metrics include Pearson correlation coefficient (r), coefficient of determination (R^2), and root mean square error (RMSE). The dashed line is the 1:1 line; the solid grey and black lines are the linear regressions fitted to all data and to the masked data, respectively.

GLEAM account for a broader range of stress factors affecting $ET_{c\ act}$, which may collectively lead to lower $ET_{c\ act}$ estimates compared to AGRHYD.

Furthermore, it is important to restate once again that neither WaPOR nor GLEAM provides crop-specific $ET_{c\ act}$ estimates. WaPOR adopts a crop-oriented classification by distinguishing between rainfed and irrigated croplands, while GLEAM classifies vegetation into short and tall canopy groups. These classification schemes introduce discrepancies through spatial averaging across multiple vegetation types or crops within a pixel. This limitation is particularly pronounced for GLEAM, where the coarse spatial resolution of approximately 11 km implies that the reference pixels used for wheat $ET_{c\ act}$ comparison represents mixed land cover rather than exclusively wheat fields.

In contrast, AGRHYD estimates $ET_{c\ act}$ for individual crops, each

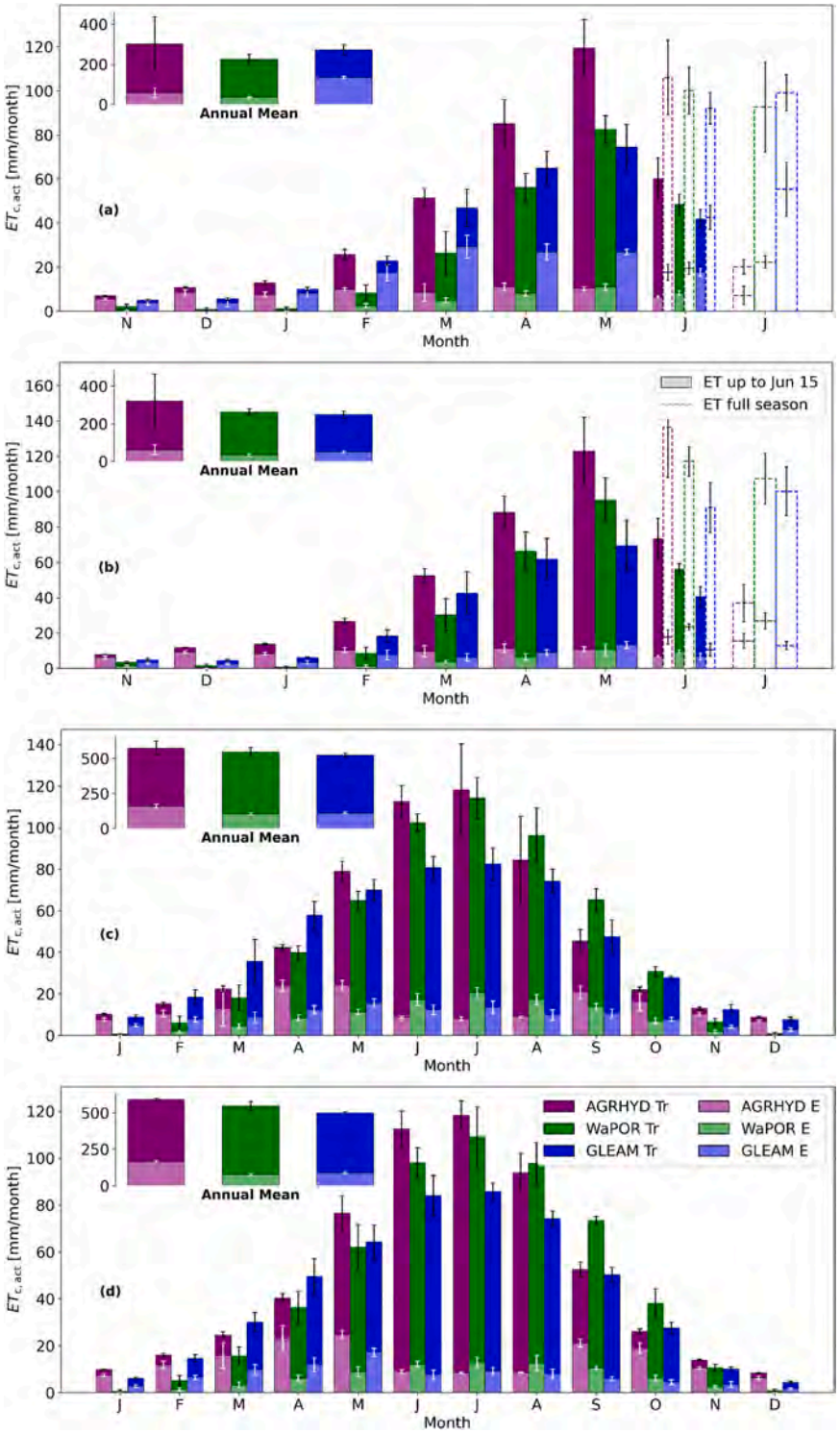


Fig. 7. Mean monthly and annual $ET_{c\ act}$ for (a)-(b) wheat reference pixels W1, W7, (c)-(d) vine reference pixels V1, and V2 as representatives from AGRHYD, WaPOR, and GLEAM during 2018–2022. Bars are partitioned into soil evaporation (*E*, lighter shades) and plant transpiration (*Tr*, darker shades). For wheat, months are arranged according to the growing season (November–July). Insets (top left) show mean annual $ET_{c\ act}$ (mm yr^{-1}).

characterized by specific phenology and crop parameters. Rooting depth, for annual crops like wheat, increases progressively during crop development, allowing access to deeper soil moisture and supporting higher *Tr* rates, whereas perennial crops such as vine maintain more stable rooting characteristics. Differences in rooting depth representation among datasets can therefore considerably affect $ET_{c\ act}$ estimates. In addition, crop rotation and temporal changes in field distribution further complicate evaluation for annual crops when land cover information is inconsistent across datasets. Despite these limitations, overall model performance remains satisfactory.

4.1.4. Seasonal comparison with WaPOR and GLEAM

Results were aggregated to monthly and annual $ET_{c\ act}$ to examine differences between AGRHYD and the reference datasets at temporal scales more relevant for water resources management. Fig. 7 presents the results for four representative reference pixels and fig.SM3 presents the results for the other reference pixels.

For wheat (Fig. 7a-b and fig. SM3 a-e), mean monthly $ET_{c\ act}$ from AGRHYD were in good agreement with GLEAM from November to March (initial-development stage) while WaPOR $ET_{c\ act}$ were negligible for most of these period (November-January) and it starts rising from February and thus much smaller than both AGRHYD and GLEAM in February-March. In April and May (late development and mid growing stage) when crop water consumption is at its maximum, the rate of $ET_{c\ act}$ significantly increased for ARGHYD making it larger than the other two. This was followed by decline in $ET_{c\ act}$ in all three datasets where in several cases this synchrony was observed up to June 15 (late mid-stage) only.

Separation of *E* and *Tr* components indicated that AGRHYD *E* was in good agreement with both WaPOR and GLEAM throughout the growing season, with an overall stronger agreement with GLEAM which can be attributed to their similar water balance concepts. However, within November-January (initial-early and development growing stage), the *Tr* share in reference datasets was low, particularly for WaPOR, most likely reflecting the dormancy period which is better captured by remote sensing products. From February onward, *Tr* was consistently larger in AGRHYD compared to both reference datasets. This can be attributed to two factors not similarly represented in WaPOR and GLEAM: (i) a crop-specific rooting depth that increases linearly within wheat development in AGRHYD, enabling greater soil water extraction from deeper layers, and (ii) the reliance of AGRHYD on soil moisture availability as the primary stress factor unlike the reference datasets which incorporate multiple stress factors (Section 4.1.3), that further constrain *Tr*. *Tr* values from February to June were more comparable between AGRHYD and WaPOR while GLEAM showed lower *Tr* and larger *E* values, attributable to the coarser spatial resolution of GLEAM which averages different vegetation cover (reducing *Tr*) while capturing a larger proportion of exposed soil surfaces (increasing *E*).

For vine (Fig. 7c-d and fig. SM3), distinct patterns were observed across the three datasets. Overall AGRHYD $ET_{c\ act}$ showed closer agreement with GLEAM during dormant period (November to February) and with WaPOR within the active period (March to October). AGRHYD *E* was comparable to both reference datasets, particularly GLEAM, throughout the year with exception of April and May where AGRHYD *E* was larger. This can be attributed to the increase in ET_0 during this period while the fraction of exposed soil is still larger than the mid-season thus higher *E* in AGRHYD. AGRHYD *Tr* was broadly consistent with WaPOR throughout the year while in June and July, corresponding to the growing stage where crop water demand is maximum, AGRHYD *Tr* exceeded both reference datasets, particularly GLEAM.

For both crops, interannual variability in *E* remained low across all months compared to *Tr* which showed greater variability during the mid-season stage in AGRHYD. This period corresponds to peak *Tr* demand, when soil moisture availability, the primary stress factor in AGRHYD, becomes critical producing a stronger interannual response. In contrast, the multiple stress factors incorporated in WaPOR and GLEAM buffer these fluctuations (Section 4.1.3), explaining the lower *Tr* variability in the reference datasets.

At the annual scale, a very good agreement was found among all three datasets for both crops with mean annual $ET_{c\ act}$ values falling within a comparable range across AGRHYD, WaPOR, and GLEAM.

Overall, despite some differences in *E* and *Tr*, the main $ET_{c\ act}$ dynamics captured by both WaPOR and GLEAM were adequately reproduced by AGRHYD, with strong agreement at both seasonal and annual scales most relevant for water resources management. Consistent evaluation against two independent reference datasets with different methodological frameworks provides confidence in the reliability of AGRHYD for regional crop water use assessments.

4.2. Irrigation requirements of Maize and Forages

The spatial distribution of mean annual *IR* for maize and forages averaged for pixels over the period 1981–2022 is shown in Fig. 8. The basin-wide average *IR* for maize was 243 mm yr^{-1}, with considerable spatial variability ranging from 3 to 353 mm yr^{-1} and for forages was 264 reaching over 500 in some areas. The highest *IR*, defined as the upper quartile for maize (>297 mm yr^{-1}), were concentrated in eastern Piedmont and central-north in Emilia-Romagna while for forages (>330 mm yr^{-1}) were concentrated in the same areas plus central Piedmont. In these hotspot areas, *IR* corresponded to the lowest precipitation and highest ET_0 (Fig. 8). Conversely, the lowest *IR* values were observed along the perimeter of the basin which are adjacent to the mountains.

These results were compared with *IR* estimates reported for the Po River Basin and northern Italy in previous studies, prioritising those with finer spatial resolution for a more accurate comparison. (Wriedt et al., 2009) provided mean annual *IR* estimates across the basin for all irrigated crops excluding rice at spatial resolution of 10 km for the period 1995–2002. Since maize and forages constitute a very large share of irrigated crops in the area, their results were considered relatively suitable for comparison with ours. The reported values ranged from 251 to 500 mm yr^{-1} across most of the basin in line with our estimates and above 500 mm yr^{-1} in eastern Piedmont and Emilia-Romagna, consistent with the *IR* hotspots identified in the present study. The closest and most relevant comparison is with recent AIDA dataset (Galli et al., 2025) at 1 km spatial resolution specifically provided for Italy. For the overlapping period 2013–2022 across the basin, AIDA reported a mean annual *IR* of 215 mm yr^{-1} for maize, compared to 275 mm yr^{-1} in the present study. This difference is primarily attributable to the dual-K_c framework employed in AGRHYD, which explicitly accounts for topsoil evaporation and its replenishment by irrigation, a component absent in the single-K_c approach employed for AIDA. For fodder crops, the closest AIDA category to our forages, AIDA reported a mean annual IR of 252 mm yr^{-1} compared to 267 mm yr^{-1} in our study, a notably smaller difference of 6%. This smaller difference is consistent with the more continuous canopy cover of perennial forage crops, which reduces the relative contribution of *E* and thereby narrows the gap between dual- and single-K_c approaches. Importantly, AIDA corroborates the spatial patterns identified here, confirming that *IR* hotspots for both crops are concentrated in eastern Piedmont and the central-northern part of Emilia-Romagna.

4.3. Trend analysis

To estimate the spatio-temporal trend of *IR*, the non-parametric Theil-Sen estimator was employed at each pixel for each crop for 1981–2022. The statistical significance of the trend at each pixel was assessed using the Trend-Free Pre-whitening Maan-Kendall test with Yue's modification (TFPW-Y; (Yue et al., 2002)), which accounts for the interaction between trend and autocorrelation by removing the trend before pre-whitening the series, thereby avoiding inflation of the test statistic. Despite the negligible temporal autocorrelation, TFPW-Y was

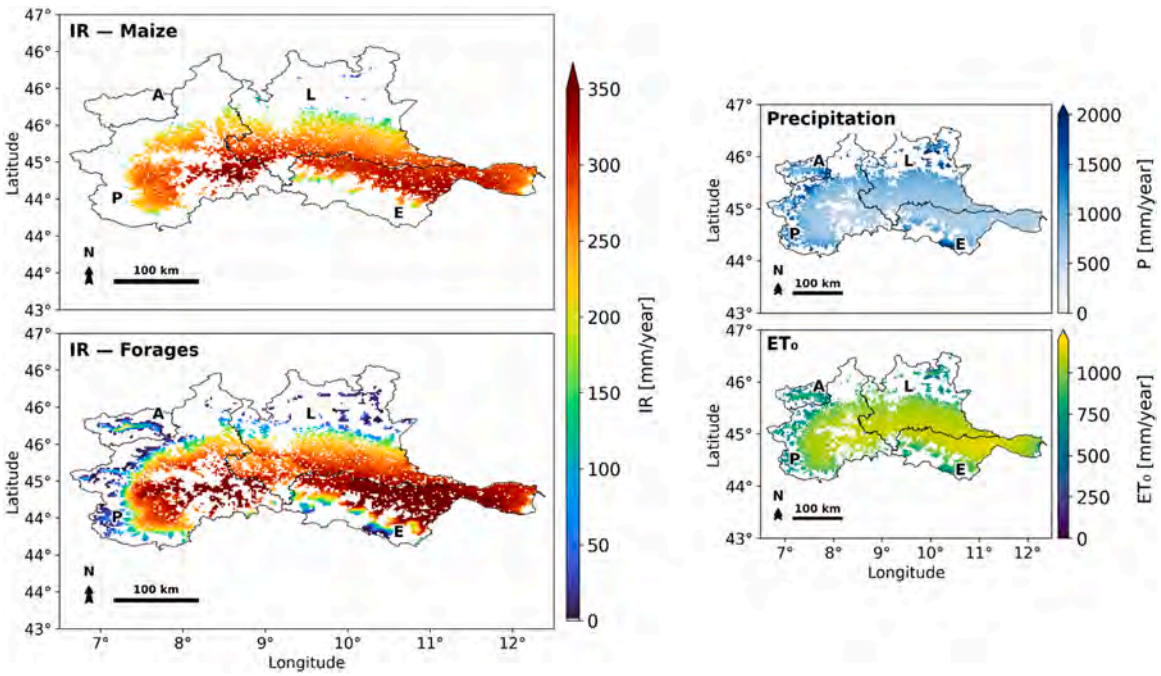


Fig. 8. Spatial distribution of mean annual *IR* (mm yr^{-1}) of maize and forages, Precipitation, and ET_0 (mm yr^{-1}) over irrigated areas in the Po Basin (1981–2022). White areas represent non-irrigated land for maize and forages; black lines show regions boundaries. A, P, L, E stand for regions Aosta Valley, Piedmont, Lombardy, and Emilia-Romagna, respectively.

nonetheless employed as it is more robust than the standard Maan-Kendall test in the presence of monotonic trends regardless of autocorrelation structure. To control the false discovery across the large number of pixels tested simultaneously, the Benjamini-Hochberg correction (Benjamini and Hochberg, 1995) was applied to the pixel-wise p-values at $\alpha = 0.05$. The trend analysis was conducted using *IR* depth (mm) and not the volumetric one since the irrigated area map was created based on data on one year thus making it misleading for a temporal analysis.

The analysis of annual *IR* trends over the period 1981–2022 indicated statistically significant increasing trends for both crops across the majority of irrigated area pixels where *IR* increased at the mean rate of $+1.55 \pm 0.50$ mm yr^{-1}. For maize, *IR* increased at a mean rate of $+1.43 \pm 0.35$ mm yr^{-1} across 3506 statistically significant pixels (45% of maize area), with local maxima reaching $+2.64$ mm yr^{-1}. For forages, mean increases of $+1.66 \pm 0.59$ mm yr^{-1} were detected across 3957 statistically significant pixels (38% of forages area), reaching local maxima of $+3.55$ mm yr^{-1} (Fig. 9). Basin spatial mean *IR* showed significant increasing trends of 0.88 mm yr^{-1} for maize and 1.17 mm yr^{-1} for forages (Fig. 10).

4.3.1. *Seasonal irrigation requirements trends*

To investigate the seasonal drivers of annual increases in *IR*, the same trend analysis was applied at the monthly scale and the results are presented for both crops combined. Statistically significant positive trends were identified mainly in April, June, and July, while in May and

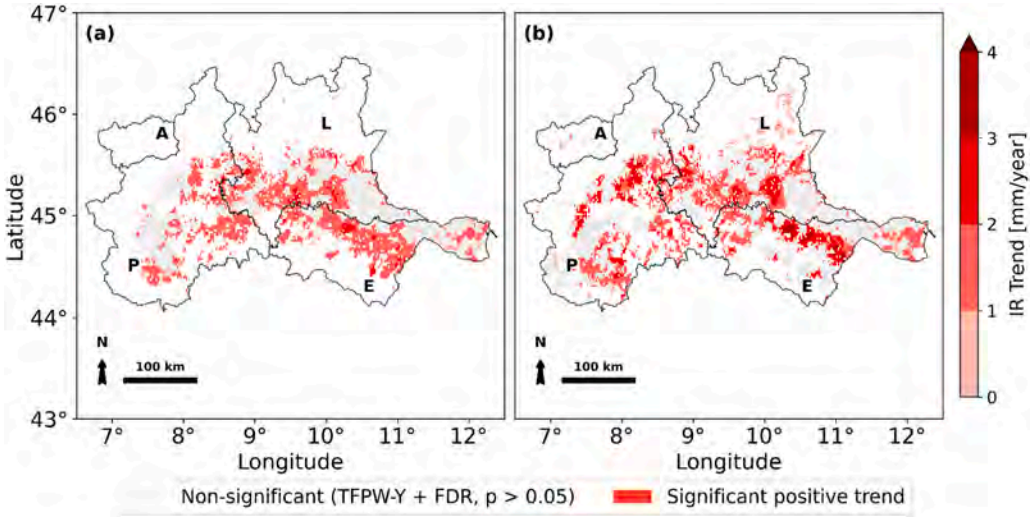


Fig. 9. Annual *IR* trends (mm yr^{-1}) for (a) maize and (b) forages in the Po River Basin for 1981–2022. Red areas indicate statistically significant increasing trends; grey areas show non-significant trends. White areas represent non-irrigated area; black lines show regions boundaries. A, P, L, E stand for regions Aosta Valley, Piedmont, Lombardy, and Emilia-Romagna, respectively.

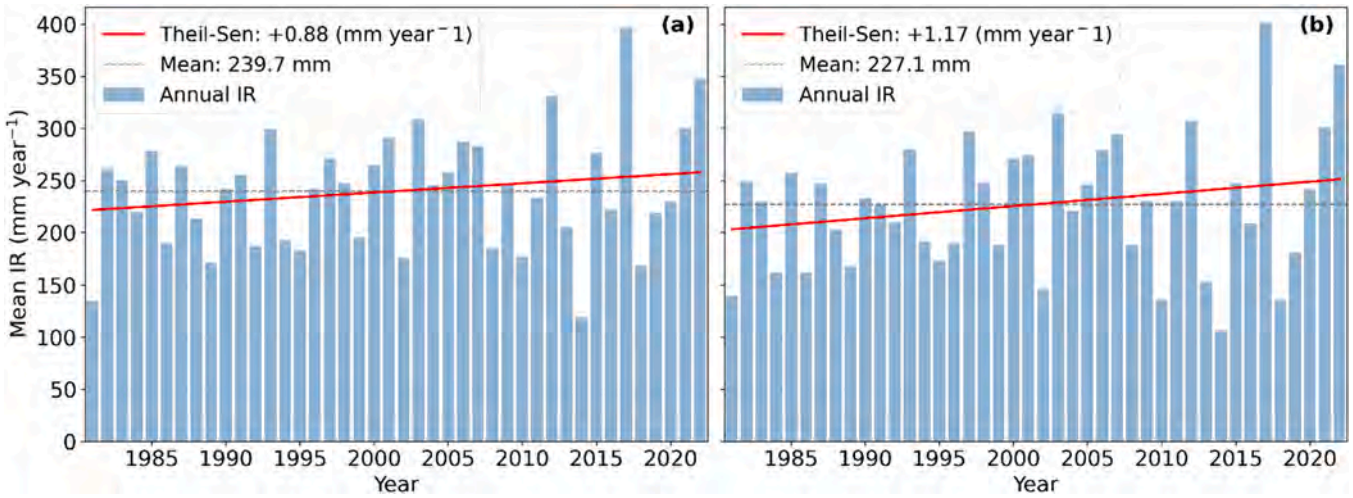


Fig. 10. Basin-wide mean annual *IR* (mm yr^{-1}) for maize (a) and forages (b) over the Po River Basin for 1981–2022. The red line shows the statistically significant trends slope and dashed grey line indicates the long-term mean.

August only limited areas showed significant trends of both positive and negative sign, predominantly driven by forages (Fig. 11). In April, significant positive trends were detected across 5393 statistically significant pixels (about 50% of total area with non-zero *IR*) with a mean rate of +0.13 ± 0.08 mm yr^{-1}. Trends intensified markedly moving towards the peak growing season (June-July), both in magnitude and spatial extent. In June, the combined mean trend reached +0.84 ± 0.33 mm yr^{-1} across 5830 significant pixels (53% of total area with non-zero *IR*), with maize and forages showing mean rates of +0.80 ± 0.30 mm yr^{-1} and + 0.93 ± 0.40 mm yr^{-1}, respectively. In July, the combined mean trend reached +0.68 ± 0.37 mm yr^{-1} across 6113 significant pixels (56% of total area with non-zero *IR*), the largest spatial extent of any month, with maize showing +0.59 ± 0.22 mm yr^{-1} and forages +0.73 ± 0.40 mm yr^{-1}.

For forages only, significant positive trends of limited spatial extent were detected in May and August, with mean rates of +0.23 ± 0.43 mm yr^{-1} in May, concentrated in southern Lombardy and Emilia-Romagna, and +0.33 ± 0.46 mm yr^{-1} in August, predominantly along the western perimeter of the basin in Piedmont and central Emilia-Romagna. Significant negative trends of limited spatial extent and magnitude were also detected in May and August, while more dominant negative trends emerged in September (mean: −0.27 ± 0.30 mm yr^{-1}) and October (mean: −0.22 ± 0.10 mm yr^{-1}), mainly concentrated in Emilia-Romagna (fig. SM5).

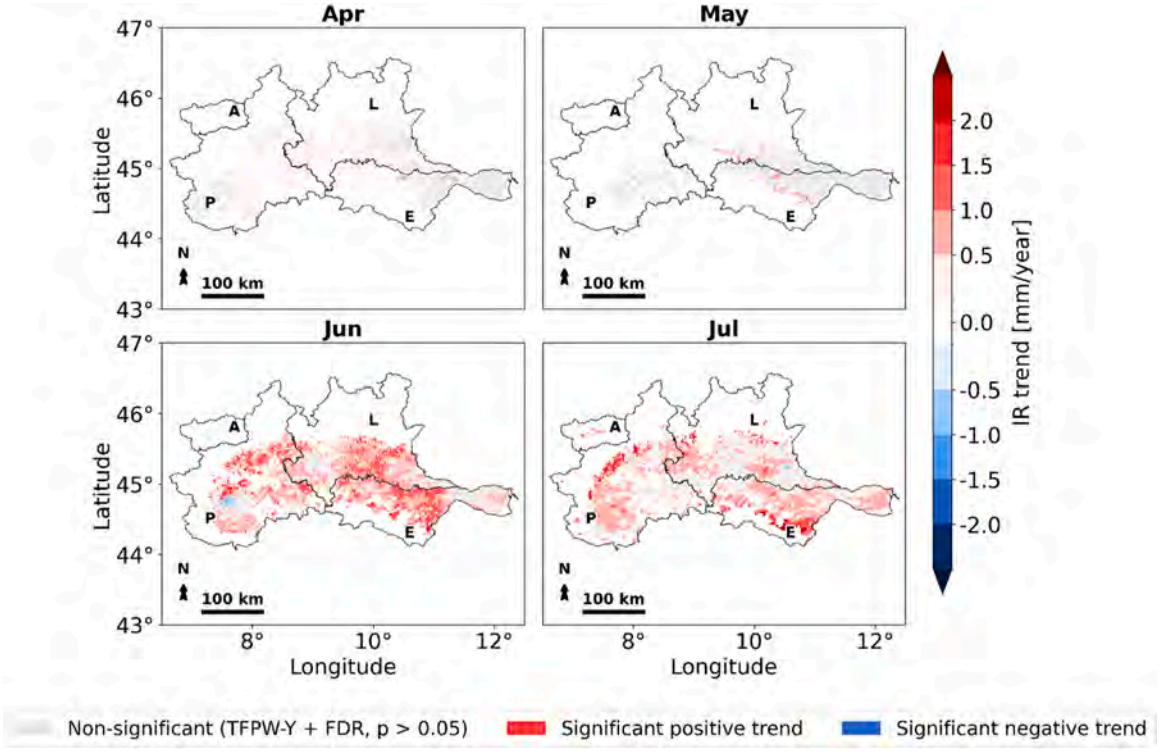


Fig. 11. Monthly *IR* trends across the Po River Basin for combined maize and forages in critical months (1981–2022). Spatial maps show Theil-Sen slopes for pixels with statistically significant trends. White areas represent non-irrigated area; black lines show regions boundaries. A, P, L, E stand for regions Aosta valley, Piedmont, Lombardy, and Emilia-Romagna, respectively.

Across both crops, June and July emerged as the dominant months driving the positive annual *IR* trend.

4.3.2. Sensitivity of irrigation requirements trends to crop calendar uncertainty

To assess the robustness of the *IR* trends analysis to uncertainty in crop calendar timing, four additional simulations were performed by shifting the growing season by ± 10 and ± 20 days relative to the original calendar. The resulting monthly Theil-Sen slopes for combined maize and forages for significant pixels are compared across all five simulations in Fig. 12.

June and July, which were identified as the primary drivers of the annual *IR* increase, showed the highest stability across all calendar shift scenarios. For June, median slopes ranged narrowly from +0.70 to +0.85 mm yr^{-1}, with a maximum deviation from the original median (+0.82 mm yr^{-1}) of +0.11 mm yr^{-1}. July showed even greater stability, with median slopes ranging from +0.55 to +0.61 mm yr^{-1} and a maximum deviation of just +0.05 mm yr^{-1} from the original (+0.60 mm yr^{-1}). While the number of significant pixels showed some variation across scenarios, the median slope magnitudes remained stable, confirming that the direction and approximate magnitude of peak-season *IR* trends are robust to crop calendar uncertainty.

For April, May, and August which showed lower trends both in magnitude and spatial extent, the median slope showed higher sensitivity to calendar shift scenarios.

April showed moderate sensitivity, with earlier growing season shifts amplifying the trend magnitude and later growing season shifts reducing both the slope and the number of significant pixels markedly. This reflects the fact that April captures the beginning of the irrigation season, where a shift in crop calendar directly determines how much of the early irrigation demand falls within this month.

May and August showed crop-specific sensitivity patterns worth examining separately (fig. SM6). In May, the signal was driven almost entirely by forages. Shifting the growing season earlier placed more developed crop growth stages, with higher crop coefficients and greater water demand, resulting in both stronger positive median slopes (up to +0.50 mm yr^{-1} for − 20 days) and a larger number of significant pixels (n = 1311). Conversely, shifting the growing season later postponed these more demanding growth stages keeping May within the earlier, less water-demanding crop growth stages which reduced the median slope and the number of significant pixels monotonically from 724 in the original to 457 in the + 20 days scenario. Notably, although the median slope turned negative under the + 10 and + 20 days scenarios, a considerable portion of the trends remained positive suggesting that the negative signal reflects a shift in the dominant pattern rather than a complete reversal across the landscape.

In August, maize and forages showed distinct sensitivity patterns. For maize, August sits at the late growing season, and the sensitivity followed a clear monotonic pattern where earlier growing season shifts progressively reduced both the median slope and the number of significant pixels with no significant pixels at all under the − 20 days scenario, as the late-season water demand moved into July. Conversely, later growing season shifts kept more of the maize peak demand within August producing stronger positive trends (median = +0.49 mm yr^{-1}) despite a reduced number of significant pixels overall.

For forages, four of the five scenarios produced consistent positive medians ranging from +0.42 to +0.54 mm yr^{-1}. The exception was the − 10 days shift, which produced a low negative median (−0.08 mm yr^{-1}). Spatial inspection of the trend maps revealed that this anomaly reflects a diffuse pattern of small-magnitude negative trends spread across the areas where late season is in the first half of August. The reason is likely caused by the fact that earlier growing season shift bringing the late-season crop water demand decline from August into July mostly and leaving only the last 5 days of the season in August which have very low water demand and thus reducing the trends in general in August. For − 20 days, the growing season ends entirely within July for these areas, leaving no late-season contribution to August, which explains why this scenario rejoins the other positive scenarios with a lower but consistent pixel count.

Overall, the sensitivity analysis confirms that the key findings of Section 4.3.1, the dominant and spatially extensive increasing *IR* trends in June and July, are robust across the range of plausible crop calendar assumptions, providing confidence in the reliability of the trend analysis despite uncertainty in the precise timing of the growing season.

4.3.3. Seasonal precipitation and reference crop evapotranspiration trends

Monthly trends in precipitation and ET_o were analysed over the combined irrigated area of maize and forages for April–July, consistent with the months exhibiting the most significant *IR* trends, to assess whether the climate drivers are coherent with the *IR* trends. Across all months, and on average precipitation consistently exhibited negative trends while ET_o showed positive trends, indicating a concurrent reduction in rainfall supply and increase in atmospheric demand over the irrigated landscape (Figs. 13 and 14).

In April, significant negative precipitation trends were identified across 65.6% of the irrigated area, with a mean of −0.89 ± 0.39 mm yr^{-1}. In May, precipitation trends were spatially inconsistent covering 32.3% of the irrigated area (mean: −0.10 ± 0.95 mm yr^{-1}),

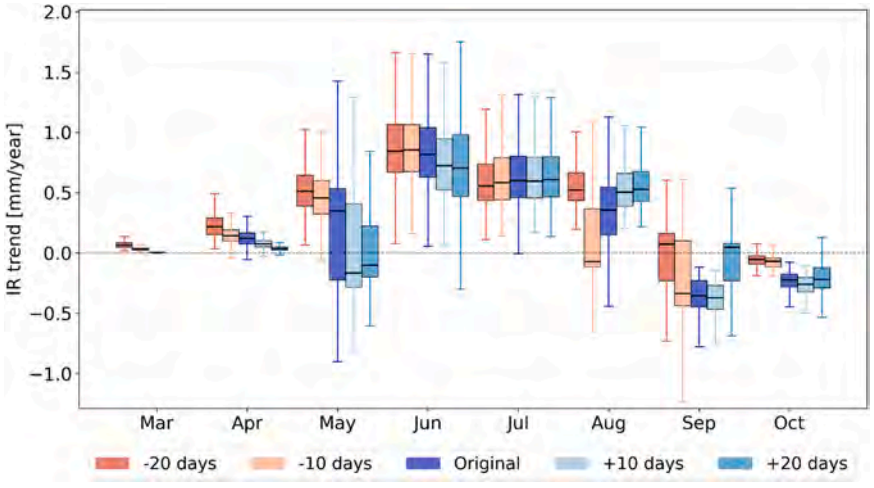


Fig. 12. Monthly *IR* statistically significant trends slopes (mm yr^{-1}) for the combined maize and forages irrigated areas across the Po River Basin for the period 1981–2022, shown for five crop calendar scenarios: the original calendar and shifts of ±10 and ±20 days.

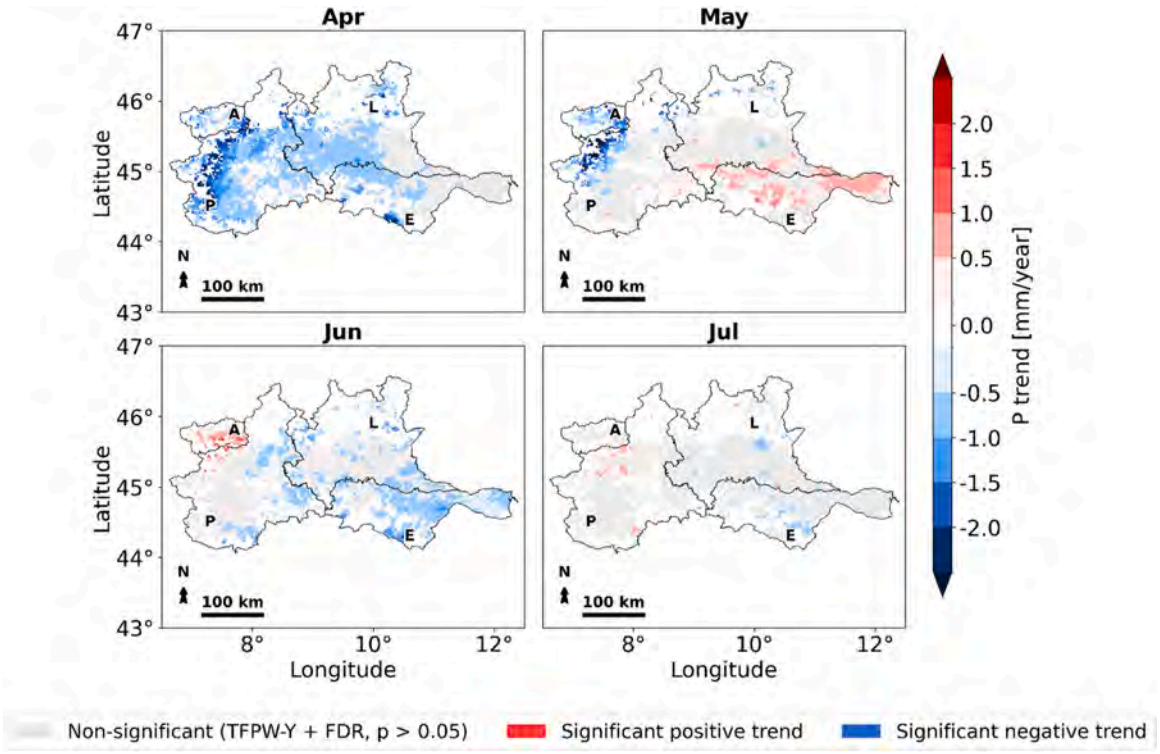


Fig. 13. Monthly precipitation (*P*) trends across the Po River Basin (1981–2022) for April, May, June, and July. red indicates significant positive trends, blue indicates significant negative trends, and gray indicates non-significant areas. White areas represent non-irrigated area; black lines show regions boundaries. A, P, L, E stand for regions Aosta valley, Piedmont, Lombardy, and Emilia-Romagna, respectively.

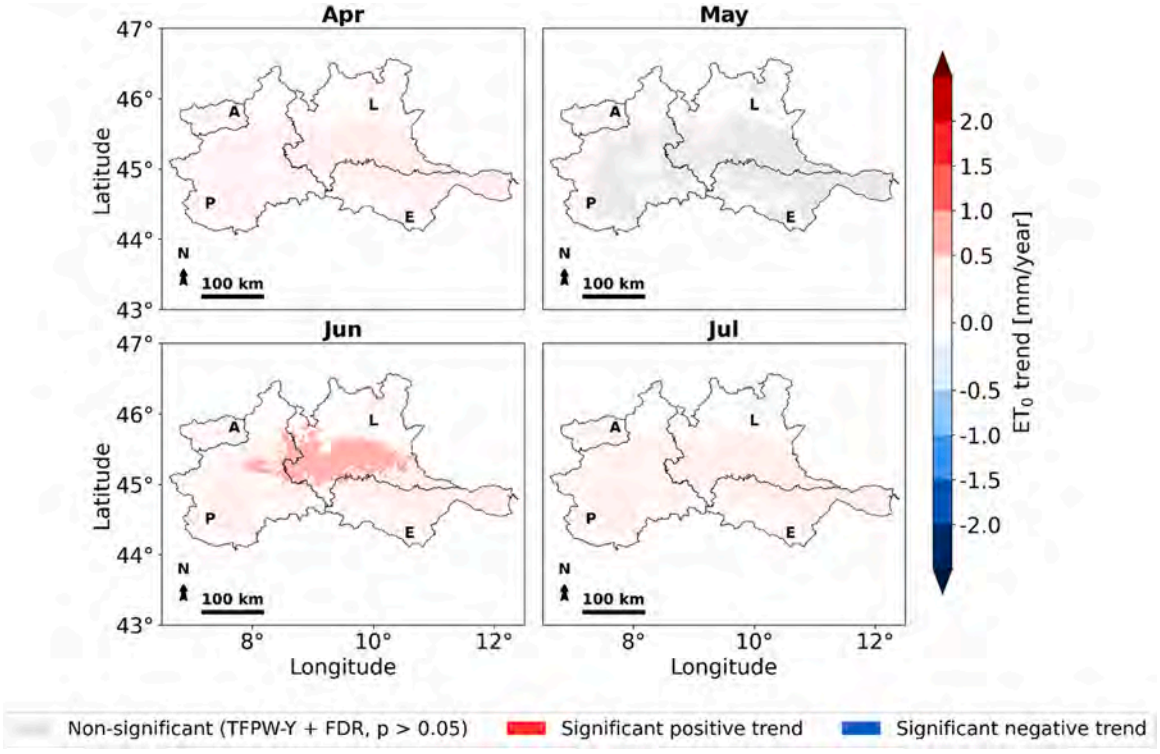


Fig. 14. Monthly ET_0 trends across the Po River Basin (1981–2022) for April, May, June, and July. Red indicates significant positive trends, blue indicates significant negative trends, and gray indicates non-significant areas. White areas represent non-irrigated area; black lines show regions boundaries. A, P, L, E stand for regions Aosta valley, Piedmont, Lombardy, and Emilia-Romagna, respectively.

with positive signals in Emilia-Romagna and negative signals mainly in Aosta valley and western Piedmont. In June, significant negative precipitation trends covered 47% of the irrigated area (mean: −0.50 ± 0.43 mm yr^{-1}) with the exception of positive trends in the Aosta

valley. In July, both the spatial extent and magnitude decreased markedly with significant trends confined to 12.8% of the irrigated area and a mean of -0.14 ± 0.48 mm yr^{-1}.

For ET_o, significant positive trends in April and June were remarkably widespread, covering almost the entire irrigated area. The mean trend increased from $+0.24 \pm 0.04$ mm yr^{-1} in April to $+0.43 \pm 0.09$ mm yr^{-1} in June, with the strongest signals concentrated in Lombardy, reflecting an intensification of atmospheric evaporative demand when moving towards the peak growing season. July also showed near-complete spatial coverage with a mean $+0.22 \pm 0.04$ mm yr^{-1}. May was the exception, with only 13% of irrigated area showing significant ET_o trends, consistent with the spatially limited *IR* trends observed in this month.

Overall, the seasonal pattern of climatic trends indicated that decreases in precipitation and increases in ET_o were most pronounced and spatially coherent during April and June. The concurrence of reduced precipitation and increased atmospheric evaporative demand during these months is broadly consistent with the intensification of *IR* trends observed in the same period, with the strongest synchrony occurring in June, which corresponds on average to the peak of growing season for both crops across the basin. The near-complete spatial coverage of significant ET_o trends in April, June and July suggests that the increasing atmospheric evaporative demand may be a dominant basin-wide driver of the observed *IR* increases, while the more spatially variable and locally contrasting precipitation trends suggest that precipitation changes likely play a secondary and more localised role.

The contribution of precipitation and ET_o trends to the estimated *IR* trends is of clear physical relevance, as reduced precipitation and increased atmospheric evaporative demand are the primary climatic drivers of irrigation demand. However, *IR* is not simply or linearly linked to precipitation and ET_o, given that it is estimated through a SWB model in which several other factors intervene: soil water storage capacity, crop development stage, irrigation triggering rules, soil moisture memory, and the lag between a rainfall event and its effect on soil moisture as well as the time required for soil moisture to fall below the threshold that triggers irrigation. A thorough attribution analysis of the *IR* trend to its climatic drivers is therefore beyond the scope of this study. Nonetheless, a basin-wide comparison of annual time series of *IR*, precipitaiton and ET_o, computed as spatial means over the total irrigated area and correlated using Pearson's correlation coefficient (r), revealed a strong and statistically significant correlations in all four months April-July (fig. SM7). *IR* showed strong negative correlations with *P* across all months ($r = -0.78$, -0.60, -0.61, and -0.85 for April, May, June and July, respectively), indicating that drier years consistently drive higher *IR*. Equally strong positive correlations were found between *IR* and ET_o ($r = +0.83$, $+0.60$, $+0.85$ and $+0.84$ for April, May, June, and July respectively), confirming that years with higher atmospheric evaporative demand correspond to higher *IR*.

Overall, these results suggest that the observed long-term increases in *IR* are at least partly driven by the combined effect of declining precipitation and rising atmospheric evaporative demand, especially during the peak growing season, even if the precise quantitative contribution of each driver cannot be disentangled within the modelling framework used here.

Several limitations of this study should be acknowledged. Maize crop coefficients and phenological parameters, although extracted from local field studies (Facchi et al., 2013), were applied uniformly across the basin, introducing uncertainty into the *IR* estimates that is difficult to quantify without spatially distributed field-scale observations across the basin. The use of fixed crop calendars over the entire 42-year period does not account for potential long-term shifts in sowing and harvesting dates that may have occurred in response to climate change. While the sensitivity analysis performed here by shifting the crop calendar confirmed that the key trend findings, particularly in June and July, are robust to such uncertainties, spatially and temporally varying phenological changes remain unaccounted for and represent a direction for future investigation. The current version of AGRHYD model considers water stress as the sole limiting factor on crop water use, excluding other stressors such as nutrient deficiency, heat stress, and pest pressure that may influence $ET_{c\ act}$ under field conditions. Finally, the absence of direct in-situ measurements of $ET_{c\ act}$ and soil moisture across the study area precluded a more direct validation of the model outputs, with the evaluation relying entirely on satellite-based reference datasets that carry their own uncertainties. These limitations are largely inherent to long-term regional modelling under data-scarce conditions and reflect necessary assumptions given the spatial and temporal scope of the study.

Beyond the methodological limitations outlined above, the scope of this study was limited to maize and forages and did not include rice, one of the most extensively irrigated crops in certain localised areas of the basin, along with other crops. Extending the framework to these crops represents a priority for future work to provide a more complete picture of Po River Basin irrigation demand.

5. Conclusions

This study presented AGRHYD, a spatially distributed agro-hydrological model built on the FAO 56 dual-K_c framework with refinements to soil evaporation estimation and a more physically explicit representation of soil moisture, as a parsimonious yet physically consistent framework for estimating $ET_{c\ act}$, ET_c, and *IR* at regional scale. Despite its modest data requirements, the model demonstrated strong agreement with two independent satellite-based evapotranspiration products derived from more complex modelling frameworks. Applied over 42 years across the Po River Basin for maize and forages, two of the most extensively irrigated crops in the region, AGRHYD delivered long-term crop-specific daily *IR* estimates at 2.2 km spatial resolution. Future work should though extend the crop coverage to other irrigated crops in the area and explore satellite soil moisture assimilation to further constrain soil evaporation estimates and reduce uncertainty on the simulated $ET_{c\ act}$ and *IR*.

Model evaluation provided evidence for the reliability of the *IR* estimates, and long-term trend analysis revealed statistically significant increases in *IR* for both crops, consistent with concurrent declines in precipitation and rising atmospheric evaporative demand. These findings, although limited to maize and forages, are particularly relevant in the context of the broader water resource pressures facing the region, given that these two crops constitute a large share of the irrigated area and are widespread across the Po River Basin. The region already faces mounting pressure on its water resources, as local irrigation practices remain relatively inefficient, snowmelt contributions are declining under climate change, and water demand is increasing. The results presented here, consistent with independent estimates from previous studies, corroborate the severity of this situation and reinforce the urgency of forward-looking adaptation strategies. From a water resource management perspective, the long-term crop-specific *IR* estimates at the temporal and spatial resolution produced here provide actionable guidance for irrigation scheduling and water allocation planning across this strategically important region, both from an economic standpoint and in terms of food supply chains at the national and continental scale.

CRediT authorship contribution statement

Amirarsalan Shahmohammadi: Writing – original draft, Methodology, Formal analysis, Data curation, Conceptualization. **Stefania Tamea:** Writing – review & editing, Supervision, Methodology, Funding acquisition, Conceptualization.

Declaration of Generative AI and AI-assisted technologies in the writing process

During the preparation of this work the authors used Claude (Anthropic) to assist with phrasing and improve the readability of the

manuscript. After using this tool/service, the authors reviewed and edited the content as needed and takes full responsibility for the content of the published article.

Declaration of Competing Interest

The authors declare that they have no known competing financial interests or personal relationships that could have appeared to influence the work reported in this paper.

Acknowledgments

This study was funded by the ClimaXPo project "CLIMate Adaptation for the PO river basin district" (LIFE21-IPC-IT-LIFE-CLIMAX-PO, project n.101069928).

Appendix A. Supporting information

Supplementary data associated with this article can be found in the online version at doi:10.1016/j.agwat.2026.110887.

Data availability

The 2.2 km resolution daily irrigation requirements dataset for maize and forages over the Po River Basin (1981–2022) generated in this study is publicly available on Zenodo at https://doi.org/10.5281/zenodo.23573249.

References

Adinolfi, M., Raffa, M., Reder, A., Mercogliano, P., 2023. Investigation on potential and limitations of ERA5 Reanalysis downscaled on Italy by a convection-permitting model. Clim. Dyn. 61, 4319–4342.

Allen, R.G., Pereira, L.S., Raes, D., Smith, M., 1998. FAO Irrigation and drainage paper No. 56. Rome Food Agric. Organ. U. N. 56, e156.

Amazirh, A., Merlin, O., Er-Raki, S., Bouras, E., Chehbouni, A., 2021. Implementing a new texture-based soil evaporation reduction coefficient in the FAO dual crop coefficient method. Agric. Water Manag. 250, 106827.

Aus der Beek, T., Flörke, M., Lapola, D., Schaldach, R., Voß, F., Teichert, E., 2010. Modelling historical and current irrigation water demand on the continental scale: Europe. Adv. Geosci. 27, 79–85.

Bastiaanssen, W.G.M., Ahmad, M.-D., Chemin, Y., 2002. Satellite surveillance of evaporative depletion across the Indus Basin. Water Resour. Res. 38, 9-1–9-9. https://doi.org/10.1029/2001WR000386.

Baumert, J., Heckelei, T., Storm, H., 2024. Probabilistic crop type mapping for ex-ante modelling and spatial disaggregation. Ecol. Inform. 83, 102836. https://doi.org/10.1016/j.ecoinf.2024.102836.

Beck, H.E., Zimmermann, N.E., McVicar, T.R., Vergopolan, N., Berg, A., Wood, E.F., 2018. Present and future Köppen-Geiger climate classification maps at 1-km resolution. Sci. Data 5, 1–12.

Benjamini, Y., Hochberg, Y., 1995. Controlling the False Discovery Rate: A Practical and Powerful Approach to Multiple Testing. J. R. Stat. Soc. Ser. B Stat. Methodol. 57, 289–300. https://doi.org/10.1111/j.2517-6161.1995.tb02031.x.

Berti, A., Tardivo, G., Chiaudani, A., Rech, F., Borin, M., 2014. Assessing reference evapotranspiration by the Hargreaves method in north-eastern Italy. Agric. Water Manag. 140, 20–25. https://doi.org/10.1016/j.agwat.2014.03.015.

Braden, H., 1985. Ein energiehaushalts-und verdunstungsmodell for wasser und stoffhaushaltsuntersuchungen landwirtschaftlich genutzer einzugsgebiete. Mittel Dtsch. Bodenkd. Geselschaft 42, 294–299.

Carlson, G., Massari, C., Rotiroti, M., Bonomi, T., Preziosi, E., Wilder, A., Whitaker, D., Girotto, M., 2025. Intensive irrigation buffers groundwater declines in key European breadbasket. Nat. Water 110.

Chapagain, A.K., Hoekstra, A.Y., 2004. Water Footpr. Nations.

Cid, P., Taghvaeian, S., Hansen, N.C., 2018. Evaluation of the Fao-56 Methodology For Estimating Maize Water Requirements Under Deficit And Full Irrigation Regimes In Semiarid Northeastern Colorado. Irrig. Drain. 67, 605–614. https://doi.org/10.1002/ird.2245.

Cook, E., 2022. Key Figures on the European Food Chain: 2022 Edition. Publications Office of the European Union.

Copernicus Land Monitoring Service, 2017a. Leaf Area Index 2014-present (raster 300 m), global, 10-daily - version 1. https://doi.org/10.2909/219FDC9F-616B-444B-A495-198F527B4722.

Copernicus Land Monitoring Service, 2017b. Fraction of Vegetation Cover 2014-present (raster 300 m), global. https://doi.org/10.2909/09578C73-4F5D-4D2C-90FF-4E17FB7DBF69.

Copernicus Land Monitoring Service, 2021. Crop Types 2021 (raster 10 m), Europe, yearly.

d'Andrimont, R., Verhegghen, A., Lemoine, G., Kempeneers, P., Meroni, M., Van Der Velde, M., 2021. From parcel to continental scale – A first European crop type map based on Sentinel-1 and LUCAS Copernicus in-situ observations. Remote. Sens. Environ. 266, 112708. https://doi.org/10.1016/j.rse.2021.112708.

De Lannoy, G.J., Bechtold, M., Busschaert, L., Heyvaert, Z., Modanesi, S., Dunmire, D., Lievens, H., Getirana, A., Massari, C., 2024. Contributions of irrigation modeling, soil moisture and snow data assimilation to high-resolution water budget estimates over the Po basin: Progress towards digital replicas. J. Adv. Model. Earth Syst. 16, e2024MS004433.

Dias Lopes, J., Neiva Rodrigues, Lineu, Acioli Imbuzeiro, Hewlley Maria, Falco Pruski, F., 2019. Performance of SSEBop model for estimating wheat actual evapotranspiration in the Brazilian Savannah region. Int. J. Remote. Sens. 40, 6930–6947. https://doi.org/10.1080/01431161.2019.1597304.

Döll, P., Siebert, S., 2002. Global modeling of irrigation water requirements. Water Resour. Res. 38, 8. –1.

Dong, J., Zhu, Y., Jia, X., Shao, M., Han, X., Qiao, J., Bai, C., Tang, X., 2022. Nation-scale reference evapotranspiration estimation by using deep learning and classical machine learning models in China. J. Hydrol. 604, 127207.

Droogers, P., Allen, R.G., 2002. Estimating Reference Evapotranspiration Under Inaccurate Data Conditions. Irrig. Drain. Syst. 16, 33–45. https://doi.org/10.1023/A:1015508322413.

El-Magd, I.A., Tanton, T., 2005. Remote sensing and GIS for estimation of irrigation crop water demand. Int. J. Remote. Sens. 26, 2359–2370. https://doi.org/10.1080/0143116042000298261.

Eurostat, S.E., 2019. Agric. -Environ. Indic. Irrig.

Facchi, A., Gharsallah, O., Corbari, C., Masseroni, D., Mancini, M., Gandolfi, C., 2013. Determination of maize crop coefficients in humid climate regime using the eddy covariance technique. Agric. Water Manag. 130, 131–141. https://doi.org/10.1016/j.agwat.2013.08.014.

FAO, 2020. The State of Food and Agriculture 2020. FAO.

FAO, 2020b. WaPOR database methodology. Version 2 release, April 2020, 1st ed. FAO, Rome, Italy. https://doi.org/10.4060/ca9894en.

FAO, 2023. Remote sensing determination of evapotranspiration–Algorithms, strengths, weaknesses, uncertainty and best fit-for-purpose. Cairo.

FAO, 2024. World Food and Agriculture – Statistical Yearbook 2024, FAO Statistical Yearbook – World Food and Agriculture. FAO, Rome, Italy. https://doi.org/10.4060/cd2971en.

Feng, J., Wang, W., Xu, F., Wang, S., 2024. Evaluating the ability of deep learning on actual daily evapotranspiration estimation over the heterogeneous surfaces. Agric. Water Manag. 291, 108627.

Fereres, E., Soriano, M.A., 2007. Deficit irrigation for reducing agricultural water use. J. Exp. Bot. 58, 147–159. https://doi.org/10.1093/jxb/erl165.

Fischer, G., Nachtergaele, F.O., Van Velthuizen, H., Chiozza, F., Francheschini, G., Henry, M., Muchoney, D., Tramberend, S., 2021. Global agro-ecological zones (gaez v4)-model documentation.

Folhes, M., Rennó, C., Soares, J., 2009. Remote sensing for irrigation water management in the semi-arid Northeast of Brazil. Agric. Water Manag. 96, 1398–1408.

Food and Agriculture Organization of the United Nations, 2020. World food and agriculture-statistical yearbook 2020. Food and Agriculture Organization of the United Nations.

Galli, N., Nanesha, H., Tolazzi, A., Chiarelli, D.D., Rulli, M.C., 2025. The AIDA 1 km resolution crop-specific rainfed and irrigated areas and green and blue water demands for Italy. Sci. Data 12, 1041. https://doi.org/10.1038/s41597-025-05390-1.

García-Gutiérrez, V., Stöckle, C., Gil, P.M., Meza, F.J., 2021. Evaluation of Penman-Monteith Model Based on Sentinel-2 Data for the Estimation of Actual Evapotranspiration in Vineyards. Remote. Sens. 13, 478. https://doi.org/10.3390/rs13030478.

Gavin, H., Agnew, C.A., 2004. Modelling actual, reference and equilibrium evaporation from a temperate wet grassland. Hydrol. Process. 18, 229–246. https://doi.org/10.1002/hyp.1372.

Geng, Q., Zhao, Y., Sun, S., He, X., Wang, D., Wu, D., Tian, Z., 2023. Spatio-temporal changes and its driving forces of irrigation water requirements for cotton in Xinjiang, China. Agric. Water Manag. 280, 108218. https://doi.org/10.1016/j.agwat.2023.108218.

Granata, F., Zhu, S., Di Nunno, F., 2025. Hydrological extremes in the Mediterranean basin: interactions, impacts, and adaptation in the face of climate change. Reg. Environ. Change 25, 100. https://doi.org/10.1007/s10113-025-02432-7.

Hersbach, H., Bell, B., Berrisford, P., Hirahara, S., Horányi, A., Muñoz-Sabater, J., Nicolas, J., Peubey, C., Radu, R., Schepers, D., Simmons, A., Soci, C., Abdalla, S., Abellan, X., Balsamo, G., Bechtold, P., Biavati, G., Bidlot, J., Bonavita, M., De Chiara, G., Dahlgren, P., Dee, D., Diamantakis, M., Dragani, R., Flemming, J., Forbes, R., Fuentes, M., Geer, A., Haimberger, L., Healy, S., Hogan, R.J., Hólm, E., Janisková, M., Keeley, S., Laloyaux, P., Lopez, P., Lupu, C., Radnoti, G., de Rosnay, P., Rozum, I., Vamborg, F., Villaume, S., Thépaut, J.-N., 2020. The ERA5 global reanalysis. Q. J. R. Meteorol. Soc. 146, 1999–2049. https://doi.org/10.1002/qj.3803.

Hillel, D., Hatfield, J.L., Powlson, D., Rosenzweig, C., Scow, K., Singer, M., 2005. Encycl. Soils Environ. 4 vols.

Italian National Institute of Statistics, 2021. The 7th Italian Agricultural Census.

Ma, Y., Sun, S., Li, C., Zhao, J., Li, Z., Jia, C., 2023. Estimation of regional actual evapotranspiration based on the improved SEBAL model. J. Hydrol. 619, 129283. https://doi.org/10.1016/j.jhydrol.2023.129283.

Marin, F.R., Angelocci, L.R., Nassif, D.S.P., Vianna, M.S., Pilau, F.G., da Silva, E.H.F.M., Sobenko, L.R., Gonçalves, A.O., Pereira, R.A.A., Carvalho, K.S., 2019. Revisiting the crop coefficient–reference evapotranspiration procedure for improving irrigation

management. Theor. Appl. Climatol. 138, 1785–1793. https://doi.org/10.1007/s00704-019-02940-7.
McColl, K.A., 2020. Practical and Theoretical Benefits of an Alternative to the Penman-Monteith Evapotranspiration Equation. Water Resour. Res. 56, e2020WR027106. https://doi.org/10.1029/2020WR027106.
Merlin, O., Al Bitar, A., Rivalland, V., Béziat, P., Ceschia, E., Dedieu, G., 2011. An analytical model of evaporation efficiency for unsaturated soil surfaces with an arbitrary thickness. J. Appl. Meteorol. Climatol. 50, 457–471.
Mialyk, O., Schyns, J.F., Booij, M.J., Su, H., Hogeboom, R.J., Berger, M., 2024. Water footprints and crop water use of 175 individual crops for 1990–2019 simulated with a global crop model. Sci. Data 11, 206.
Miralles, D.G., Bonte, O., Koppa, A., Baez-Villanueva, O.M., Tronquo, E., Zhong, F., Beck, H.E., Hulsman, P., Dorigo, W., Verhoest, N.E.C., Haghdoost, S., 2025. GLEAM4: global land evaporation and soil moisture dataset at 0.1° resolution from 1980 to near present. Sci. Data 12, 416. https://doi.org/10.1038/s41597-025-04610-y.
Montanari, A., Nguyen, H., Rubinetti, S., Ceola, S., Galelli, S., Rubino, A., Zanchettin, D., 2023. Why the 2022 Po River drought is the worst in the past two centuries. Sci. Adv. 9, eadg8304. https://doi.org/10.1126/sciadv.adg8304.
Natural Resources Conservation Service, 1997. National Engineering Handbook, Part 652, Irrigation Guide. Unknown. https://doi.org/10.22004/AG.ECON.338974.
Nie, W., Zaitchik, B.F., Rodell, M., Kumar, S.V., Arsenault, K.R., Badr, H.S., 2021. Irrigation water demand sensitivity to climate variability across the contiguous United States. Water Resour. Res. 57, 2020WR027738.
Oliveira, W.K.M., Maggi, M.F., Venancio, L.P., Bazzi, C.L., Nóbrega, L.H.P., Oliveira, A.S. D.M., Mercante, E., Schenatto, K., 2024. Remote Sensing-Based Algorithms for Estimating Evapotranspiration in Agricultural Systems: A systematic literature review. IEEE Geosci. Remote. Sens. Mag. 12, 190–217. https://doi.org/10.1109/MGRS.2024.3469182.
Olivera-Guerra, L.-E., Laluet, P., Altés, V., Ollivier, C., Pageot, Y., Paolini, G., Chavanon, E., Rivalland, V., Boulet, G., Villar, J.-M., 2023. Modeling actual water use under different irrigation regimes at district scale: Application to the FAO-56 dual crop coefficient method. Agric. Water Manag. 278, 108119.
Parmar, S.H., Patel, G.R., Tiwari, M.K., 2023. Assessment of crop water requirement of maize using remote sensing and GIS. Smart Agric. Technol. 4, 100186. https://doi.org/10.1016/j.atech.2023.100186.
Parmesan, C., Morecroft, M.D., Trisurat, Y., 2022. Clim. Change 2022 Impacts Adapt. vulnerability.
Pereira, L.S., Allen, R.G., Smith, M., Raes, D., 2015. Crop evapotranspiration estimation with FAO56: Past and future. Agric. Water Manag. Agric. Water Manag. Priorities Chall. 147, 4–20. https://doi.org/10.1016/j.agwat.2014.07.031.
Pereira, L.S., Paredes, P., Jovanovic, N., 2020. Soil water balance models for determining crop water and irrigation requirements and irrigation scheduling focusing on the FAO56 method and the dual Kc approach. Agric. Water Manag. 241, 106357. https://doi.org/10.1016/j.agwat.2020.106357.
Pereira, L.S., Allen, R.G., Paredes, P., López-Urrea, R., Raes, D., Smith, M., Kilic, A., Salman, M., 2025. Crop evapotranspiration. Guidelines for computing crop water requirements. Second edition, revised 2025, Second edition. ed, FAO Irrigation and Drainage Paper. FAO, Rome, Italy. https://doi.org/10.4060/cd6621en.
Poggio, L., de Sousa, L.M., Batjes, N.H., Heuvelink, G.B.M., Kempen, B., Ribeiro, E., Rossiter, D., 2021. SoilGrids 2.0: producing soil information for the globe with quantified spatial uncertainty. SOIL 7, 217–240. https://doi.org/10.5194/soil-7-217-2021.
Rockel, B., Will, A., Hense, A., 2008. The regional climate model COSMO-CLM (CCLM). Meteorol. Z. 17, 347.
Rockström, J., Karlberg, L., Wani, S.P., Barron, J., Hatibu, N., Oweis, T., Bruggeman, A., Farahani, J., Qiang, Z., 2010. Managing water in rainfed agriculture—The need for a paradigm shift. Agric. Water Manag. Compr. Assess. Water Manag. Agric. 97, 543–550. https://doi.org/10.1016/j.agwat.2009.09.009.
Rolle, M., Tamea, S., Claps, P., 2021. ERA5-based global assessment of irrigation requirement and validation. PLoS. One 16, e0250979.
Rolle, M., Tamea, S., Claps, P., 2022. Climate-driven trends in agricultural water requirement: an ERA5-based assessment at daily scale over 50 years. Environ. Res. Lett. 17, 044017.
Ruess, P., Konar, M., Wanders, N., Bierkens, M., 2023. Irrigation by crop in the Continental United States from 2008 to 2020. Water Resour. Res. 59, e2022WR032804.
Senay, G.B., Friedrichs, M., Morton, C., Parrish, G.E.L., Schauer, M., Khand, K., Kagone, S., Boiko, O., Huntington, J., 2022. Mapping actual evapotranspiration using Landsat for the conterminous United States: Google Earth Engine implementation and assessment of the SSEBop model. Remote. Sens. Environ. 275, 113011. https://doi.org/10.1016/j.rse.2022.113011.
Simons, G., Koster, R., Droogers, P., 2020. Hihydrosoil v2. 0-high resolution soil maps of global hydraulic properties. Future Work.
Singh, R.K., Senay, G.B., 2016. Comparison of Four Different Energy Balance Models for Estimating Evapotranspiration in the Midwestern United States. Water 8, 9. https://doi.org/10.3390/w8010009.
Sophocleous, M., 2004. Global and Regional Water Availability and Demand: Prospects for the Future. Nat. Resour. Res. 13, 61–75. https://doi.org/10.1023/B:NARR.0000032644.16734.f5.
Sumner, D.M., Jacobs, J.M., 2005. Utility of Penman–Monteith, Priestley–Taylor, reference evapotranspiration, and pan evaporation methods to estimate pasture evapotranspiration. J. Hydrol. 308, 81–104. https://doi.org/10.1016/j.jhydrol.2004.10.023.
Sun, Z., Wei, B., Su, W., Shen, W., Wang, C., You, D., Liu, Z., 2011. Evapotranspiration estimation based on the SEBAL model in the Nansi Lake Wetland of China. Math. Comput. Model. Math. Comput. Model. Agric. (CCTA 2010) 54, 1086–1092. https://doi.org/10.1016/j.mcm.2010.11.039.
Tuninetti, M., Tamea, S., D'Odorico, P., Laio, F., Ridolfi, L., 2015. Global sensitivity of high-resolution estimates of crop water footprint. Water Resour. Res. 51, 8257–8272. https://doi.org/10.1002/2015WR017148.
Verger, A., Sánchez-Zapero, J., Weiss, M., Descals, A., Camacho, F., Lacaze, R., Baret, F., 2023. GEOV2: Improved smoothed and gap filled time series of LAI, FAPAR and FCover 1 km Copernicus Global Land products. Int. J. Appl. Earth Obs. Geoinf. 123, 103479. https://doi.org/10.1016/j.jag.2023.103479.
Von-Hoyningen-Huene, J., 1983. Die interzeption des Niederschlages in landwirtschaftlichen Pflanzenbeständen.
Wang, W., Zhuo, L., Ji, X., Yue, Z., Li, Z., Li, M., Zhang, H., Gao, R., Yan, C., Zhang, P., 2023. A gridded dataset of consumptive water footprints, evaporation, transpiration, and associated benchmarks related to crop production in China during 2000–2018. Earth Syst. Sci. Data Discuss. 2023, 1–34.
Wriedt, G., Van der Velde, M., Aloe, A., Bouraoui, F., 2008. Water requirements for irrigation in the European Union. Model. Based Assess. Irrig. Water Requir. Reg. Water Demands Eur.
Wriedt, G., Van der Velde, M., Aloe, A., Bouraoui, F., 2009. Estimating irrigation water requirements in Europe. J. Hydrol. 373, 527–544.
Xiong, Y.J., Zhao, W.L., Wang, P., Paw U, K.T., Qiu, G.Y., 2019. Simple and applicable method for estimating evapotranspiration and its components in arid regions. J. Geophys. Res. Atmospheres 124, 9963–9982.
Xue, J., Fulton, A., Kisekka, I., 2021. Evaluating the role of remote sensing-based energy balance models in improving site-specific irrigation management for young walnut orchards. Agric. Water Manag. 256, 107132.
Xue, Y., Zhang, Z., Li, X., Liang, H., Yin, L., 2025. A Review of Evapotranspiration Estimation Models: Advances and Future Development. Water Resour. Manag. 1, 17.
Yan, X., Yang, N., Ao, R., Mohammadian, A., Liu, J., Cao, H., Yin, P., 2023. Deep learning for daily potential evapotranspiration using a HS-LSTM approach. Atmos. Res. 292, 106856.
Yue, S., Pilon, P., Phinney, B., Cavadias, G., 2002. The influence of autocorrelation on the ability to detect trend in hydrological series. Hydrol. Process. 16, 1807–1829. https://doi.org/10.1002/hyp.1095.